Computational Aerodynamic Simulations of an 840 ft/sec Tip Speed Advanced Ducted Propulsor Fan System Model for Acoustic Methods Assessment and Development

Daniel L. Tweedt
AP Solutions, Inc., Cleveland, Ohio

NASA STI Program . . . in Profile

Since its founding, NASA has been dedicated to the advancement of aeronautics and space science. The NASA Scientific and Technical Information (STI) program plays a key part in helping NASA maintain this important role.

The NASA STI Program operates under the auspices of the Agency Chief Information Officer. It collects, organizes, provides for archiving, and disseminates NASA's STI. The NASA STI program provides access to the NASA Aeronautics and Space Database and its public interface, the NASA Technical Reports Server, thus providing one of the largest collections of aeronautical and space science STI in the world. Results are published in both non-NASA channels and by NASA in the NASA STI Report Series, which includes the following report types:

- TECHNICAL PUBLICATION. Reports of completed research or a major significant phase of research that present the results of NASA programs and include extensive data or theoretical analysis. Includes compilations of significant scientific and technical data and information deemed to be of continuing reference value. NASA counterpart of peer-reviewed formal professional papers but has less stringent limitations on manuscript length and extent of graphic presentations.

- TECHNICAL MEMORANDUM. Scientific and technical findings that are preliminary or of specialized interest, e.g., quick release reports, working papers, and bibliographies that contain minimal annotation. Does not contain extensive analysis.

- CONTRACTOR REPORT. Scientific and technical findings by NASA-sponsored contractors and grantees.

- CONFERENCE PUBLICATION. Collected papers from scientific and technical conferences, symposia, seminars, or other meetings sponsored or cosponsored by NASA.

- SPECIAL PUBLICATION. Scientific, technical, or historical information from NASA programs, projects, and missions, often concerned with subjects having substantial public interest.

- TECHNICAL TRANSLATION. English-language translations of foreign scientific and technical material pertinent to NASA's mission.

Specialized services also include creating custom thesauri, building customized databases, organizing and publishing research results.

For more information about the NASA STI program, see the following:

- Access the NASA STI program home page at *http://www.sti.nasa.gov*

- E-mail your question to *help@sti.nasa.gov*

- Fax your question to the NASA STI Information Desk at 443–757–5803

- Phone the NASA STI Information Desk at 443–757–5802

- Write to:
  STI Information Desk
  NASA Center for AeroSpace Information
  7115 Standard Drive
  Hanover, MD 21076–1320

Computational Aerodynamic Simulations of an 840 ft/sec Tip Speed Advanced Ducted Propulsor Fan System Model for Acoustic Methods Assessment and Development

Daniel L. Tweedt
AP Solutions, Inc., Cleveland, Ohio

National Aeronautics and
Space Administration

Glenn Research Center
Cleveland, Ohio 44135

October 2014

Level of Review: This material has been technically reviewed by NASA technical management OR expert reviewer(s).

Computational Aerodynamic Simulations of an 840 ft/sec Tip Speed Advanced Ducted Propulsor Fan System Model for Acoustic Methods Assessment and Development

Daniel L. Tweedt
AP Solutions, Inc.
Cleveland, Ohio 44135

Abstract

Computational Aerodynamic simulations of an 840 ft/sec tip speed, Advanced Ducted Propulsor fan system were performed at five different operating points on the fan operating line, in order to provide detailed internal flow field information for use with fan acoustic prediction methods presently being developed, assessed and validated. The fan system is a sub-scale, low-noise research fan/nacelle model that has undergone extensive experimental testing in the 9- by 15-foot Low Speed Wind Tunnel at the NASA Glenn Research Center, resulting in quality, detailed aerodynamic and acoustic measurement data.

Details of the fan geometry, the computational fluid dynamics methods, the computational grids, and various computational parameters relevant to the numerical simulations are discussed. Flow field results for three of the five operating conditions simulated are presented in order to provide a representative look at the computed solutions.

Each of the five fan aerodynamic simulations involved the entire fan system, excluding a long core duct section downstream of the core inlet guide vane. As a result, only fan rotational speed and system bypass ratio, set by specifying static pressure downstream of the core inlet guide vane row, were adjusted in order to set the fan operating point, leading to operating points that lie on a fan operating line and making mass flow rate a fully dependent parameter. The resulting mass flow rates are in good agreement with measurement values.

The computed blade row flow fields for all five fan operating points are, in general, aerodynamically healthy. Rotor blade and fan exit guide vane flow characteristics are good, including incidence and deviation angles, chordwise static pressure distributions, blade surface boundary layers, secondary flow structures, and blade wakes. Examination of the computed flow fields reveals no excessive boundary layer separations or related secondary-flow problems. A few spanwise comparisons between computational and measurement data in the bypass duct show that they are in good agreement, thus providing a partial validation of the computational results.

Introduction

The development and validation of aircraft engine fan acoustic prediction methods is an important part of ongoing efforts by NASA and industry to reduce noise generation in the fan section of aircraft engines. This work is part of a larger task involving computational fluid dynamics (CFD) to simulate the aerodynamics of selected fan systems, each at several different operating points, for the purpose of providing detailed internal flow field information for use with fan acoustic prediction methods presently being developed, assessed and validated.

This report documents CFD work done on one of the selected fan systems, the Advanced Ducted Propulsor (ADP) Fan, version 1, which was designed by United Technologies Corporation, Pratt & Whitney [1,2][†] with NASA funding under the Advanced Subsonic Technology program. The ADP fan is a 22-inch sub-scale, low-noise research fan/nacelle model that has undergone extensive experimental testing in the 9- by 15-foot Low Speed Wind Tunnel (LSWT) at the NASA Glenn Research Center. Several years of testing in the LSWT have produced quality, detailed aerodynamic and acoustic measurement data for the ADP fan [3][‡].

---

† Numbers in square brackets indicate references.

Fan Geometry

A meridional plane drawing of the ADP fan system is shown in Figure 1, with all major components depicted and shown to scale. The fan rotor blade stacking line is the zero-reference axial location, and the fan exit guide vane (FEGV) row is in the standard/middle configuration where its stacking line is 7.400 inches axially downstream of the rotor blade stacking line. The fan system also involves a long core-duct section (not shown) downstream of the core inlet guide vane (CIGV) row, but it was not included as part of the computational domain. The number of blades for each blade row is indicated in parenthesis. The rotating portion of the rotor hub includes the entire upstream centerbody/spinner, and extends about one inch downstream of the rotor to axial location 2.745 inches (see Figure 1, mark below hub contour downstream of rotor trailing edge).

Rotor blade coordinates for the fan were provided for the running (hot) blade shapes at the cruise operating point, which is also the aerodynamic design point. All operating points pertinent to this task involve the rotor blades in their sea-level takeoff (SLTO) configuration, which is at a blade setting angle closed 9.0 degrees from the cruise angle. At the SLTO rotational speed of 8750 rpm (mechanical and corrected), corresponding to a rotor blade tip speed of 840 ft/sec, the running blade tip deflections are expected to be very nearly the same – a difference of 0.033 degrees – as those for the fan running in the NASA GRC W8 test facility at the cruise operating point (see Table VIII in Reference 1), which is the condition at which blade fabrication coordinate corrections (hot-to-cold) were made. Therefore, the running blade shape at the SLTO condition in the NASA GRC 9- by 15-foot LSWT is, for all practical purposes and based on Reference 1, the same as that of the supplied running shape with the blade setting angle reset by a -9.0 degree coordinate rotation about the stacking axis[§].

Five aerodynamic simulation cases have been defined for the ADP fan, each at a different rotational speed on the fan operating line. In all cases mechanical speed is equal to corrected speed since the far field flow is at standard day sea-level total (stagnation) conditions. The rotor blade tip clearance at the SLTO rotational speed of 8750 rpm is specified to be 0.0200 inches. Approximate corrections to rotor blade twist and blade tip clearance were made at the other (lower) rotational speeds by assuming blade deflection to be proportional to the square of rotational speed. These results are summarized in Table 1. For blade twist corrections, the reported cold-to-hot tip untwist value (Reference 1, Table VIII) of 1.166 degrees at 8750 rpm was used to calculate the tip untwist values at the other rotational speeds. The spanwise variation in untwist was assumed to be linear, varying between zero at the hub and the calculated value at the tip. Tip clearance values were estimated based on experimental spin-test results [4] indicating an average tip radius increase of 0.0145 inches at 10,000 rpm (0.025 inches at the blade leading edge and 0.004 inches at the trailing edge).

[‡] The published data were obtained for a configuration with a takeoff-speed rotor tip clearance of 0.055 inches, which is over twice as large as the tip clearance for the current task. The experimental measurement data used for comparisons in this report are unpublished as of the report submission date.

[§] 9.0 degree clockwise rotation when viewed looking radially inward along the stacking axis.

Table 1: Rotor Blade Tip Geometry Corrections

Operating Point	Rotational Speed (rpm)	Blade Tip Untwist (degrees)	Tip Untwist Correction (degrees)	Blade Tip Clearance (inches)
SLTO	8750	1.166	0.000	0.0200
	8345	1.061	0.105	0.0210
Cutback	7525	0.862	0.304	0.0229
	6700	0.684	0.482	0.0246
Approach	5425	0.448	0.718	0.0268

The rotor hub has two clearance gaps that are separated by the blade trunnion, which extends from about 18.5 percent to 72.5 percent of blade chord. These gaps are assumed to be invariant with rotational speed. Measurements of the clearance gap heights indicate an average leading edge clearance of about 0.0135 inches, and a trailing edge clearance of about 0.0180 inches. For the CFD simulations the gap heights were approximated using a cubic polynomial for the variation of clearance between the leading and trailing edge. The trunnion location differs slightly from that of the hardware, mainly because the additional effort to generate grids conforming exactly to the hardware was not warranted. Figure 2 provides a graphical summary of the hub clearance gap height variation used for the CFD simulations.

Computational Fluid Dynamics

Two different CFD codes were used to simulate the airflow around and through the fan system: an axisymmetric viscous solver called AVCS, and a three-dimensional viscous turbomachinery solver called TSWIFT. Multiple solution domains (grid blocks) were used, with axisymmetric solutions coupled to three-dimensional solutions at mixing planes by means of a separate computer program called SMPI, developed as a companion program for AVCS and TSWIFT. SMPI was also used to couple rotating and stationary three-dimensional solutions together at mixing planes. In general, the three-dimensional TWSIFT solver was used for computational domains in and near blade rows, and the axisymmetric AVCS solver was used for computational domains sufficiently far away from blade rows[†].

The AVCS and TSWIFT codes use similar numerical algorithms; both solve the Reynolds-averaged Navier-Stokes equations on body-fitted grids using an explicit, finite-difference scheme. The codes include viscous terms in the body-normal direction(s), but neglect them in the streamwise direction by applying the thin-layer approximation. The discretized equations are solved with a multi-stage Runge-Kutta time-marching scheme using a spatially varying time step, implicit residual smoothing, and preconditioning [5-8]. All simulations described herein were run

---

[†] All program-to-program communications, for mixing planes and direct block-to-block interfaces, were handled using a facility called SYNCEX (pronounced "sink-ex"). SYNCEX is a message-passing interface that enables two or more programs to efficiently exchange data on a single computer and/or over a network.

using a 2-stage Runge-Kutta scheme with a CFL number of 2.5, and using the AUSM+ upwind scheme [9] for best accuracy.

The TSWIFT code was derived from, and has the same basic features as the SWIFT code [10] developed by Chima at the NASA Glenn Research Center. TSWIFT also has a fairly general multiblock capability (when used with SYNCEX; see preceding footnote), includes the two-equation SST turbulence model developed by Menter [11], and implements Giles' two-dimensional, steady-state, non-reflecting boundary conditions [12,13] at flow inlet, exit, and mixing-plane boundaries[†]. Note that when a two-equation turbulence model is used, either the Wilcox k-ω model [14] or the Menter SST model, it is necessary to pitchwise average the computed turbulence properties on the upstream side of the mixing plane. In that case the turbulence kinetic energy, k, and the ratio of turbulence kinetic energy to turbulence dissipation rate, k/ω, are each mass-averaged, and the resulting average values of k and (indirectly) ω are used as inflow boundary values for the domain on the downstream side of the mixing plane.

Computational Grids

An axisymmetric grid consisting of four two-dimensional grid blocks, shown in Figure 3, was used outside of the fan system blade rows. For clarity, only some of the grid lines are drawn, and the different blocks are shown in various colors: a far-field block (green), an external nacelle block (blue), an upstream/inlet block (black), and a nozzle/downstream block (black). The far-field block size is 169×45 nodes, the external nacelle block size is 297×65 nodes, and the upstream/inlet and nozzle/downstream block sizes are each 169×85 nodes. The far-field block overlaps the top of the nacelle block, but the grid nodes are not aligned, so the computational solutions are interpolated there. The bottom of the nacelle block does not overlap the upstream/inlet and nozzle/downstream blocks, but the boundary-normal grid spacings are relatively small and the boundary nodes are aligned.

The nacelle, inlet, and nozzle grid blocks were all generated using a Poisson partial differential equation (PDE) solver, otherwise known as an elliptic grid generator, which produces grids with good boundary-normal node clustering and spacings, and generally good local orthogonality. Since the CFD method always directly includes the viscous sublayer in the near-wall treatment of turbulent boundary layers – wall functions are not used – the node spacings at solid walls are small. In the inlet and on the external surface of the nacelle the wall-normal spacing is nominally 0.0001 inches, whereas in the bypass nozzle the wall-normal spacing is nominally between 0.0002 and 0.0003 inches. Corresponding inner-variable wall distances, y^+, are generally between 1.0 and 3.0.

An enlarged view of the two-dimensional grid in and around the fan system is shown in Figure 4, where every other grid line is drawn. In this figure the elliptic grid stretching for the inlet, nozzle, and nacelle grid blocks can be seen more easily. Magnified views of the grid around the nacelle leading edge and trailing edge, with every grid line drawn, are shown in Figure 5.

Meridional locations of the three-dimensional blade row grid blocks are shown in Figure 6, with flow boundaries indicated by dashed and dash-dotted lines. The blue dash-dotted lines indicate grid block direct-interfaces, and the black dashed lines indicate mixing-plane interfaces.

[†]   The SMPI code also implements Giles' two-dimensional, steady-state, non-reflecting boundary conditions.

There are four primary grid blocks for the rotor: the rotor inlet H-grid block, the rotor blade row C-grid block, the rotor exit core H-grid block, and the rotor exit bypass H-grid block. The FEGV and CIGV computational domains each involve a single C-grid block. The red streamlines in Figure 6 show stream-surface locations for blade-to-blade (streamwise-pitchwise) grid views, as well as for blade-to-blade flow contour plots, to be shown later.

The blade row grids, except for the two rotor exit H-grid blocks, were generated using a computer program called TTGRID, which is a modified version of TCGRID [15], a grid generator for turbomachinery developed by Chima at the NASA Glenn Research Center. TTGRID applies an elliptic PDE solver to the blade-to-blade mesh surfaces of blade row C- and H-grids.

Meridional plane projections of the three-dimensional blade row grid blocks at grid surfaces located about mid-pitch between the blades are shown in Figure 7, and an enlarged view of the grid blocks in the core inlet region is shown in Figure 8. Rotor grid blocks are drawn in black and green, and the FEGV and CIGV grid blocks are drawn in red. For clarity, only every other grid line in the streamwise direction is shown, although all grid lines in the spanwise direction are drawn. Corresponding three-dimensional views of the grid blocks are provided in Figures 9 and 10, again with only some of the grid lines drawn. The rotor C-grid (black) has a size of 193×49×85 nodes, the rotor inlet H-grid (green) has a size of 21×26×85 nodes, the rotor exit core H-grid (green) has a size of 49×89×53 nodes, and the rotor exit bypass H-grid (green) has a size of 69×89×73 nodes. Note that the rotor inlet H-grid overlaps the rotor blade C-grid and has node-to-node alignment with it. The rotor exit H-grids for the core and bypass also overlap the rotor blade C-grid, but the grid nodes are not aligned. On their common boundary just upstream of the flow path splitter, the two rotor exit H-grid blocks do not overlap each other, but the boundary-normal spacings are small and the nodes are aligned. The FEGV C-grid block (red) has a size of 193×45×73 nodes, and the CIGV C-grid block (red) has a size of 177×41×53 nodes. All of the three-dimensional grids have boundary-normal node spacings which are nominally 0.0002 inches at blade/vane surfaces, and 0.0003 inches at endwall surfaces.

Streamwise-pitchwise views of the rotor grid at three spanwise locations, corresponding to the red streamlines in Figure 6, are shown in Figure 11 with every other grid line drawn. Corresponding pitchwise-spanwise views of the rotor C-grid and exit H-grid at the respective block downstream boundaries are shown in Figure 12.

Over the rotor blade tip, in the endwall clearance gap, an O-grid block of size 161×13×13 nodes is used, and at the rotor hub two C-grid blocks are used in the clearance gaps, one with a size of 55×13×11 nodes for the leading clearance, and the other with a size of 63×13×11 nodes for the trailing clearance. The tip clearance grid is shown in Figure 13, which includes magnified views around the blade leading- and trailing-edges, and a magnified axial cross-section view near mid-chord. All grid lines are drawn for the magnified views. The two hub clearance grids are shown in Figure 14. Note that each of the three clearance gap grids overlaps the rotor blade C-grid and has node-to-node alignment with it.

A streamwise-pitchwise view of the FEGV grid near midspan, corresponding to the middle red streamline in Figure 6, is shown in Figure 15. Shown below the full view are magnified views of the vane leading and trailing edge regions. For clarity, only every other grid line parallel to the vane surface is drawn for the full view. A corresponding pitchwise-spanwise view of the FEGV grid at the block downstream boundary is shown in Figure 16. Lastly, a couple of representative views of the CIGV grid are shown in Figure 17.

All of the computational grid blocks and their respective sizes are summarized below in Tables 2 and 3.

Table 2: Two-Dimensional Grid Blocks

Grid Block	Size (I×J×K)	Number of Nodes
Fan System Upstream/Inlet	169×85	14,365
Fan System Nozzle/Downstream	169×85	14,365
Fan System External Nacelle	297×65	19,305
Fan System Far Field	169×45	7,605
Total All Blocks		55,640

Table 3: Three-Dimensional Grid Blocks

Grid Block	Size (I×J×K)	Number of Nodes
Rotor Inlet H-Grid	21×26×85	46,410
Rotor Blade C-Grid	193×49×85	803,845
Rotor Exit Core H-Grid	49×89×53	231,133
Rotor Exit Bypass H-Grid	69×89×73	448,293
Rotor Tip Clearance O-Grid	161×13×13	27,209
Rotor Hub Clearance Leading C-Grid	55×13×11	7,865
Rotor Hub Clearance Trailing C-grid	63×13×11	9,009
FEGV C-Grid	193×45×73	634,005
CIGV C-Grid	177×41×53	384,621
Total All Blocks		2,592,390

To conclude this section, the rotor exit bypass H-grid block and its relative importance to the CFD solutions will be discussed. It is perhaps apparent that this grid block involves a relatively large number of grid nodes, even though it contains no blade surfaces and is essentially just a downstream extension of the rotor blade C-grid. The higher grid density is necessary, however, to provide the numerical resolution needed for accurate wake convection, and to achieve a reasonable level of grid independence for the CFD solution. If the grid is too coarse, particularly in regions where the flow field involves large gradients and the primary flow is not aligned with the grid, then numerical dissipation is excessive and causes substantial distortion of computed local flow features. More specifically, excess artificial dissipation causes the computed wake and blade tip vortex to decay too rapidly.

If the primary purpose of the CFD simulations were only aerodynamic performance assessment and/or prediction, then the lack of local flow field accuracy in the wake region would probably not be crucial because local accuracy typically has a relatively small influence on spatially averaged performance quantities. For the current task, however, the computed rotor wake and tip-vortex structures are important because they define flow-field characteristics associated with noise generation. Particularly important are the computed flow field results at the rotor exit bypass H-grid downstream boundary (and mixing plane) since these are intended for direct use in acoustic methods assessment, research and development.

Fan System Aerodynamic Simulations

All CFD simulations were run with the far-field (free stream, flight) Mach number set at 0.100, with total (stagnation) conditions set at standard day sea-level values. The corresponding unit Reynolds number is 5.915E+05 inches^{-1}. Air is modeled as a perfect gas with a ratio of specific heats, γ, equal to 1.400.

The effects of turbulence were modeled using the two-equation SST turbulence model [11], with free stream turbulence on the far-field upstream boundary set at 0.2 percent, along with a turbulence (eddy) viscosity equal to 0.2 times the molecular viscosity, giving a turbulence length scale of 1.39E-03 inches. The corresponding turbulence kinetic energy is 5.99E-08 (dimensionless; multiply by square of free stream stagnation speed-of-sound to obtain a dimensional value)[†]. In all the cases simulated, rotor blade laminar-to-turbulent boundary layer transition occurred near the leading edge, at a location around 5 percent of blade chord.

Since the duct downstream of the CIGV row was not modeled in the CFD simulations, it was necessary to specify static pressures at the exit boundary of the CIGV grid. This was done by setting the hub static pressure at a specified value, and using simple radial-equilibrium to compute the static pressure distribution from hub to tip. At each operating point the value of the hub static pressure was determined iteratively so as to achieve the desired system bypass ratio (BPR) for that operating point. Measured and computed values of the fan (rotor) mass flow rate and the system bypass ratio are listed below in Table 4.

[†] At the fan inlet the turbulence is lower than originally intended because of turbulence decay upstream of the inlet, and because of an error in calculating the inlet boundary values so as to account for that decay. The turbulence is not so low, however, that it significantly affects the computed aerodynamics. Turbulence at the fan inlet is nominally about 0.03 percent, with a turbulence viscosity of 0.2 times the molecular viscosity and a turbulence kinetic energy of around 3.5E-08.

Table 4: Measured and Computed Fan Flow Rates and System Bypass Ratios

Operating Point	Rotational Speed (rpm)	Measured Flow Rate (lbm/sec)	Computed Flow Rate (lbm/sec)	Measured BPR	Computed BPR
SLTO	8750	79.20	79.61	11.50	11.49
	8345	75.60	76.11	11.20	11.20
Cutback	7525	68.10	68.86	10.70	10.73
	6700	60.70	61.55	10.30	10.28
Approach	5425	49.10	50.11	9.90	9.95

All five of the CFD simulation cases were run until the maximum and average (RMS) solution residuals were reduced by 4 to 5 orders of magnitude. Similar levels of convergence were obtained for performance-related quantities such as mass flow rate, average total temperature, and average total pressure. Integrated mass flow conservation discrepancies for the computed solutions are small, being everywhere less than ±0.04 percent.

The measured and computed mass flow rates in Table 4 differ at the SLTO condition by 0.52 percent, and at the approach condition by 2.06 percent. Between those two conditions the difference varies almost linearly with rotational speed. The uncertainty in measured flow rate is estimated to be at least ±0.5 percent, and could be significantly larger at the lower flow rates because the experimental values are calculated from a correlation using static pressures measured in the rotor seal cavity. There is, therefore, some uncertainty as to how much the computed and measured flow rates actually differ, so the agreement may be somewhat better or worse. In any case, the differences are not considered large enough to substantially compromise the intended use of the computational results; that is, for acoustic methods assessment, research and development.

Graphs in Figure 18 show spanwise distributions of total pressure and total temperature in the bypass duct, upstream of the FEGV, at a location 5.000 inches downstream of the rotor stacking line (see gray vertical line in Figure 1). Pitchwise mixed-out-averaged computational results are compared with rake measurement data for three of the five fan operating conditions: SLTO, cutback, and approach. As can be seen, there is generally good agreement between the computational and experimental data.

Selected results from three of the five CFD simulation cases are presented below. Flow field contour plots are presented for results at the SLTO, cutback, and approach operating points, the primary purpose being to provide a representative look at the computed solutions. More extensive and detailed flow field information can be obtained directly from the CFD grid and solution data sets, which are being made available along with this report, or which can be obtained separately upon request.

Mach number contours for the entire fan system flow field at the SLTO operating point are shown in Figure 19, where the three-dimensional blade-row solutions have been mixed-out averaged in the pitchwise direction. An enlarged view of the fan region is shown in Figure 20, and

a corresponding contour plot of turbulence kinetic energy, mass-averaged in the pitchwise direction, is shown in Figure 21.

Rotor blade-to-blade relative (rotating system) Mach number contours for the SLTO operating point are shown in Figures 22a and 22b. Figure 22a shows a near tip section at about 89 percent span from the hub, and Figure 22b shows near midspan and near hub sections at about 51 and 8 percent span, respectively (see red streamlines in Figure 6). Relative Mach number contours in and around the rotor tip and hub endwall clearance gaps are shown in Figures 23 and 24, respectively, where the tip mid-clearance-gap location is about 0.010 inches from the casing endwall, the hub mid-clearance-gap location is about 0.006 inches from the hub endwall, and the mid-chord axial location is at the rotor blade stacking line. Corresponding contours of relative Mach number at the rotor C-grid downstream boundary, located 2.500 inches downstream of the rotor stacking line, are shown in Figure 25, and contours of various flow properties at the rotor exit bypass H-grid downstream boundary, which is the downstream mixing plane, are shown in Figures 26a and 26b. Figure 26a shows relative and absolute (stationary system) Mach number contours, and Figure 26b shows entropy and turbulence kinetic energy contours. Note that the entropy is non-dimensionalized by the gas constant, R, and is zero at the upstream reference condition.

FEGV blade-to-blade absolute Mach number contours for fan operation at the SLTO operating point are shown in Figures 27a and 27b. Figure 27a shows a vane section at about 89 percent span from the hub, and Figure 27b shows vane sections at about 48 and 10 percent span (see red streamlines in Figure 6). Corresponding Mach number contours at the FEGV downstream mixing plane are shown in Figure 28.

Mach number contours for the entire fan system at the cutback operating point are shown in Figure 29, with an enlarged view of the fan region shown in Figure 30. Again, the three-dimensional blade-row solutions have been mixed-out averaged in the pitchwise direction. Corresponding rotor blade-to-blade relative Mach number contours are shown in Figures 31a and 31b, and various flow property contours at the rotor downstream mixing plane in the bypass duct are shown in Figures 32a and 32b. Flow field contours for the FEGV at cutback operation are not shown, but are aerodynamically similar to those at SLTO.

Mach number contours for the entire fan system at the approach operating point are shown in Figure 33, with Figure 34 showing an enlarged view of the fan region. Corresponding rotor blade-to-blade relative Mach number contours are shown in Figures 35a and 35b, and various flow property contours at the rotor downstream mixing plane in the bypass duct are shown in Figures 36a and 36b. Absolute Mach number contours for the FEGV are shown in Figures 37a and 37b, and in Figure 38. The computed FEGV flow field, like that for cutback operation, is aerodynamically similar to the SLTO solution, although it might be noted that the FEGV suction-surface/hub corner flow separation is significantly weaker for the approach operating point (compare Figure37 b to Figure 27b, and Figure 38 to Figure 28). In general, however, despite some non-conformity, the similar solutions show that the FEGV flow field scales more-or-less with flow rate for all simulated operating points on the fan operating line.

Concluding Remarks

The entire fan system was aerodynamically simulated for five operating points, requiring only fan rotational speed and system bypass ratio to be adjusted as the independent parameters when setting each operating point. As a result, the computed operating points lie on a fan operating line, and mass flow rate is a dependent parameter. Computed and measured fan system mass flow rates are in good agreement, indicating indirectly that the computational and experimental fan operating lines are nearly the same.

The computed blade row flow fields at all operating points are, in general and as expected, aerodynamically healthy. Rotor blade and FEGV flow characteristics are good, including incidence and deviation angles, chordwise static pressure distributions (not shown, but can be inferred from Mach number distributions), blade surface boundary layers, secondary flow structures, and blade wakes. Examination of the computed flow fields reveals no excessive or critical boundary layer separations or related secondary flow problems. A few spanwise comparisons between computational and measurement data in the bypass duct show that they are in good agreement, thus providing a partial validation of the computational results.

References

1. Hobbs, David E., Neubert, Robert J., Malmborg, Eric W., Philbrick, Daniel H., Spear, David A., "Low Noise Research Fan Stage Design," NASA Contractor Report (NASA internal use only; contains Pratt & Whitney proprietary data), March 1995.

2. Hobbs, David E., Neubert, Robert J., Malmborg, Eric W., Philbrick, Daniel H., Spear, David A., "Low Noise Research Fan Stage Design," NASA CR-195382, March 1995.

3. Jeracki, Robert J., "Comprehensive Report of Fan Performance From Duct Rake Instrumentation on 1.294 Pressure Ratio, 806 ft / sec Tip Speed Turbofan Simulator Models," NASA TM-2006-213863, February 2006.

4. Mehmed, O., Janetzke, D., "Deflection Spin Test Results of NASA/P&W Fan 1 Blades," NASA internal memorandum from Structural Dynamics Branch to Chief, Propeller and Acoustics Technology Branch, March 20, 1995.

5. Chima, R. V., "Viscous Three-Dimensional Calculations of Transonic Fan Performance," in CFD Techniques for Propulsion Applications, AGARD Conference Proceedings No. CP-510, AGARD, Neuilly-Sur-Seine, France, February 1992, pp 21-1 to 21-19 (also NASA TM-103800).

6. Chima, R. V., and Yokota, J. W., "Numerical Analysis of Three-Dimensional Viscous Flows in Turbomachinery," AIAA Journal, Vol. 28, No. 5, May 1990, pp. 798-806.

7. Tweedt, Daniel L., and Chima, Rodrick V., "Rapid Numerical Simulation of Viscous Axisymmetric Flow Fields," NASA TM-107103 (also AIAA-96-0449), November 1995.

8. Tweedt, Daniel L., Chima, Rodrick V., and Turkel, Eli, "Preconditioning for Numerical Simulation of Low Mach Number Three-Dimensional Viscous Turbomachinery Flows," NASA TM-113120 (also ICOMP-97-11 and AIAA-97-1828), October 1997.

9. Chima, R. V. and Liou, M.-S., "Comparison of the AUSM+ and H-CUSP Schemes for Turbomachinery Applications," AIAA Paper AIAA-2003-4120 (also NASA TM-2003-212457).

10. Chima, R. V., "Swift – Multiblock Analysis Code for Turbomachinery," User's Manual and Documentation, Version 300, August 2003.

11. Menter, R. F., "Two-Equation Eddy-Viscosity Turbulence Models for Engineering Applications," AIAA Journal, Vol. 32, No. 8, August 1994, pp. 1598-1605 (also NASA TM-111958).

12. Giles, Michael B., "Nonreflecting Boundary Conditions for Euler Equation Calculations," AIAA Journal, Vol. 28, No. 12, December 1990, pp. 2050-2058.

13. Giles, Michael, "UNSFLO: A Numerical Method For The Calculation Of Unsteady Flow In Turbomachinery," GTL Report No. 205, May 1991, pp. 45-56.

14. Wilcox, David C., *Turbulence Modeling for CFD*, DCW Industries, Inc., La Cañada, CA, Third edition, 2006.

15. Chima, R. V., "TCGRID 3-D Grid Generator for Turbomachinery, User's Manual and Documentation," Version 300, July, 2003.
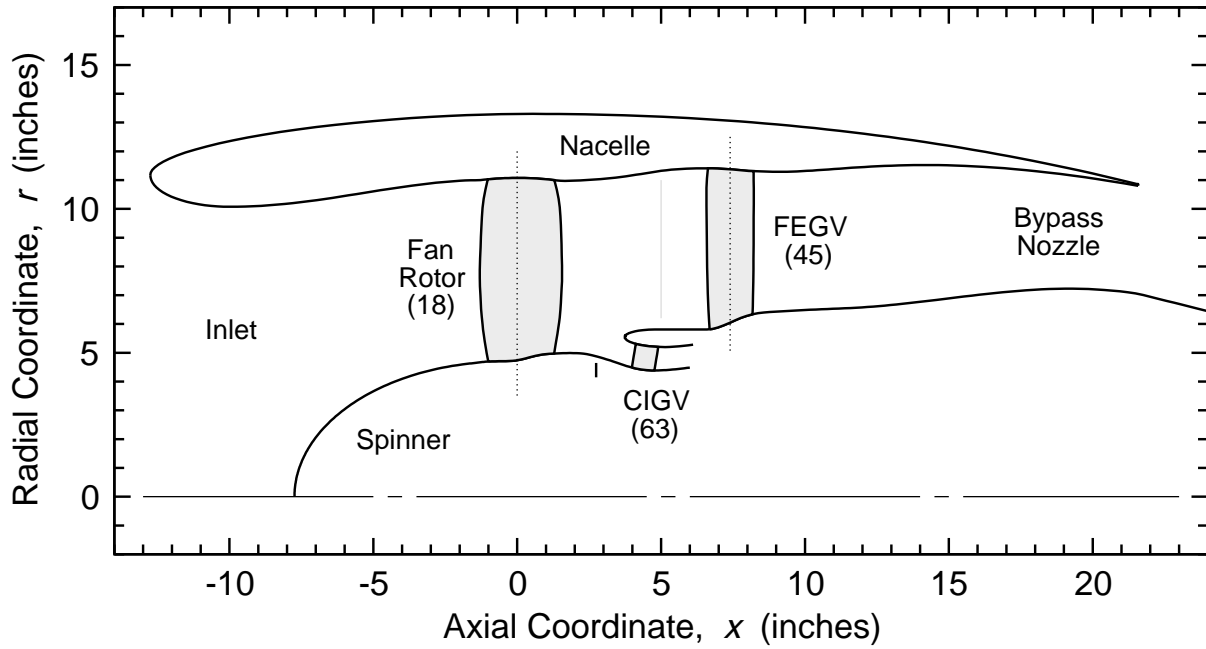
Figure 1: Schematic Drawing of the ADP Fan System
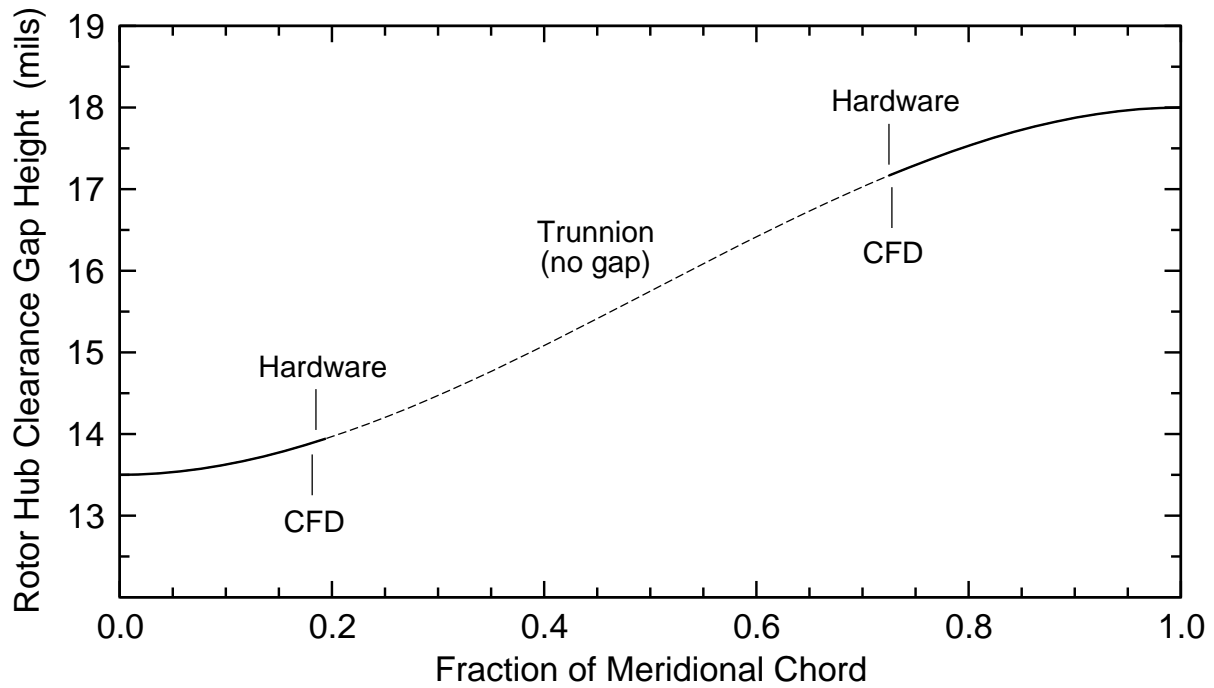
Figure 2: Rotor Hub Clearance Gap Height Variation
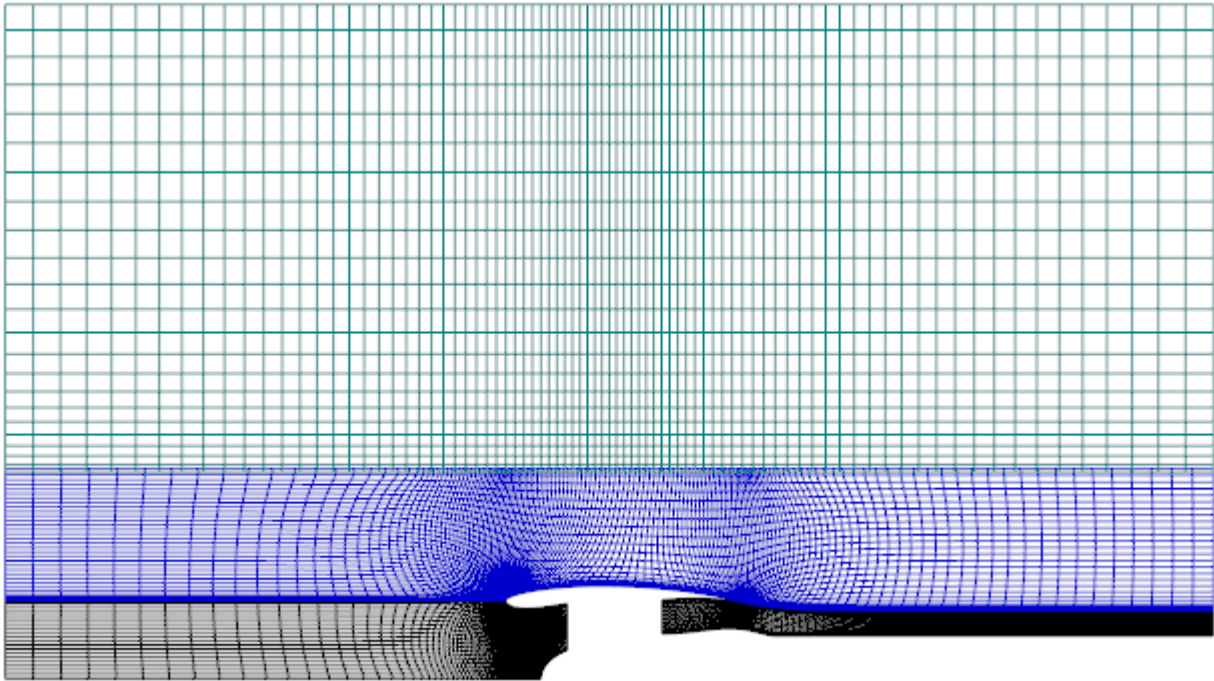
Figure 3: Two-Dimensional Axisymmetric CFD Grid Blocks (Entire Computational Domain)
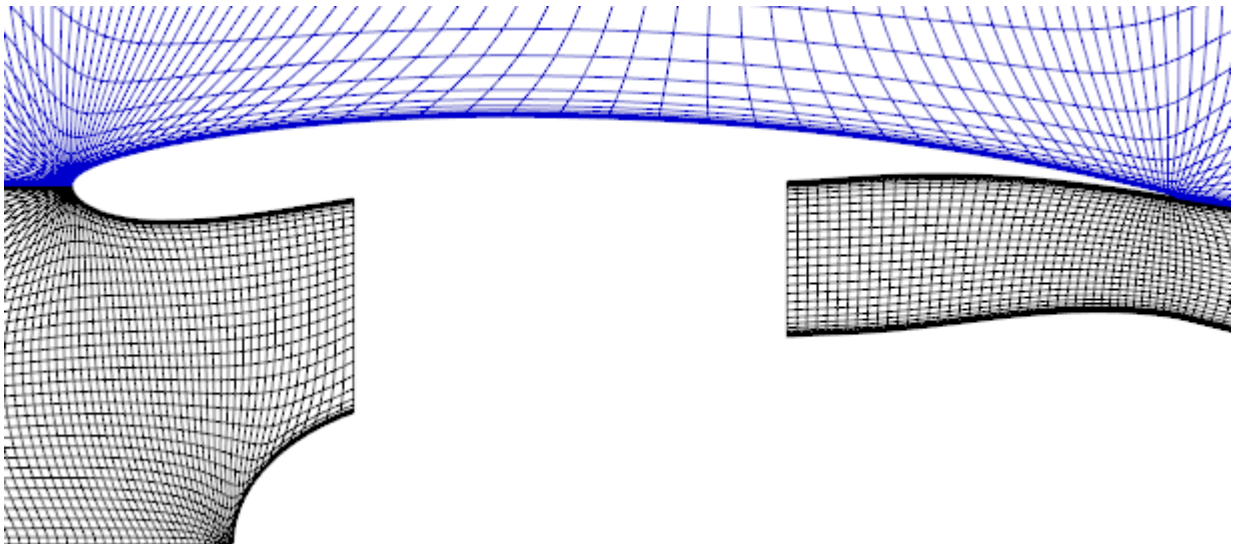
Figure 4: Enlarged Inlet, Nozzle, and Nacelle Grid Blocks
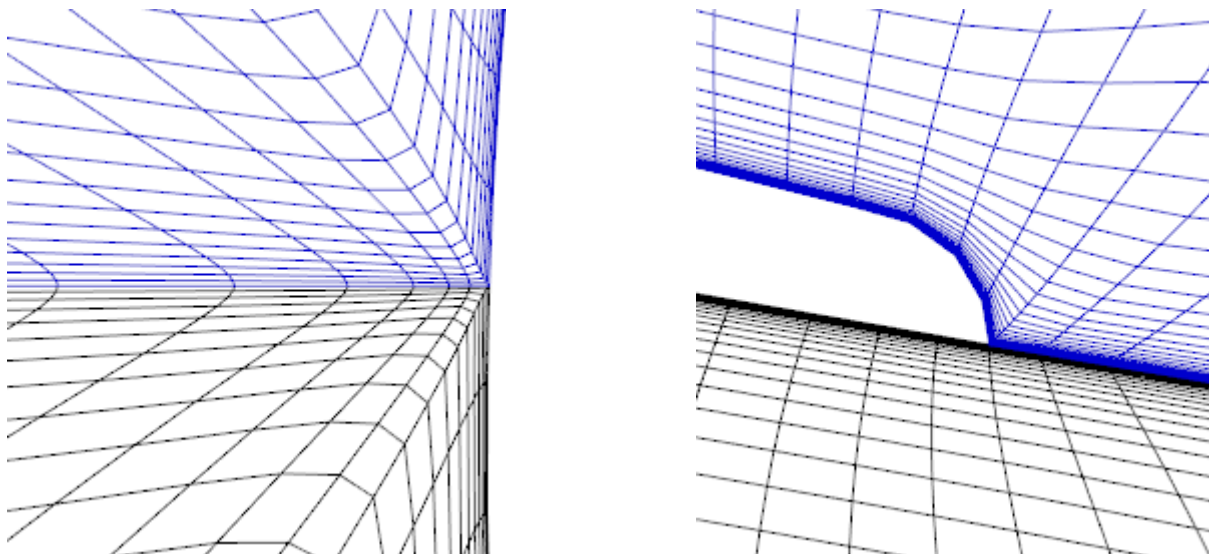
Figure 5: Magnified Nacelle Leading and Trailing Edge Grids
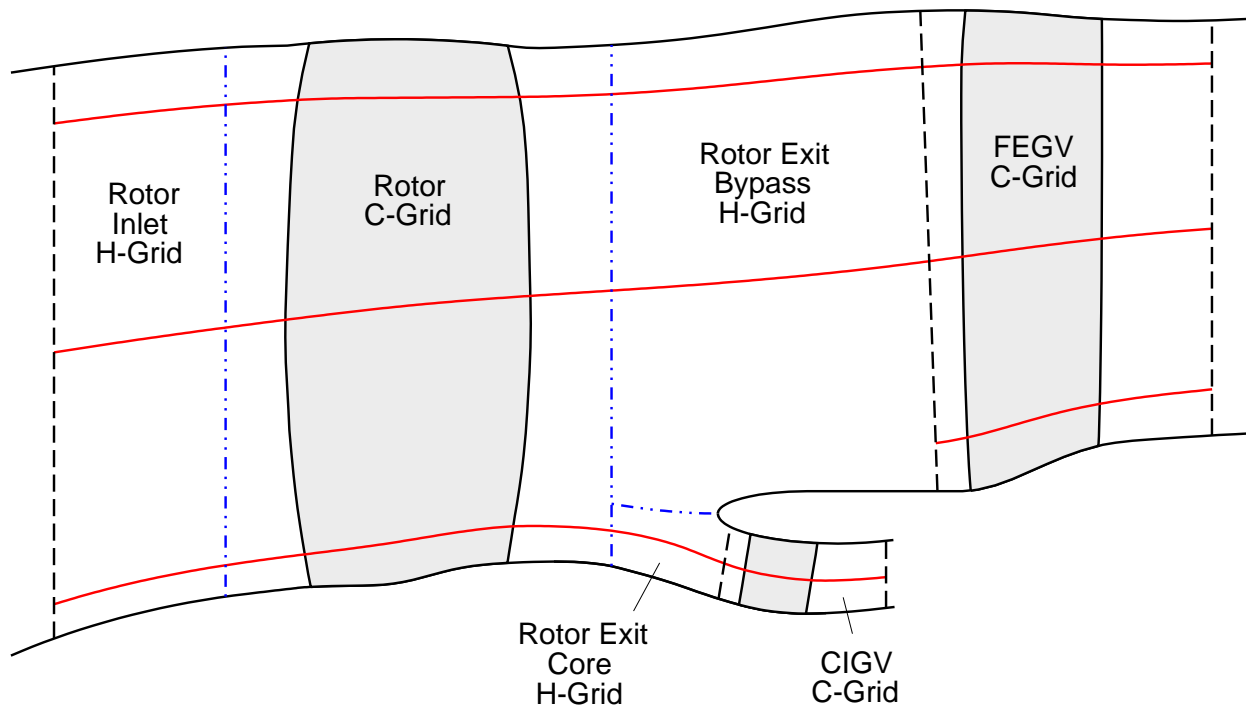
Figure 6: Meridional Location and Extent of Three-Dimensional CFD Grid Blocks
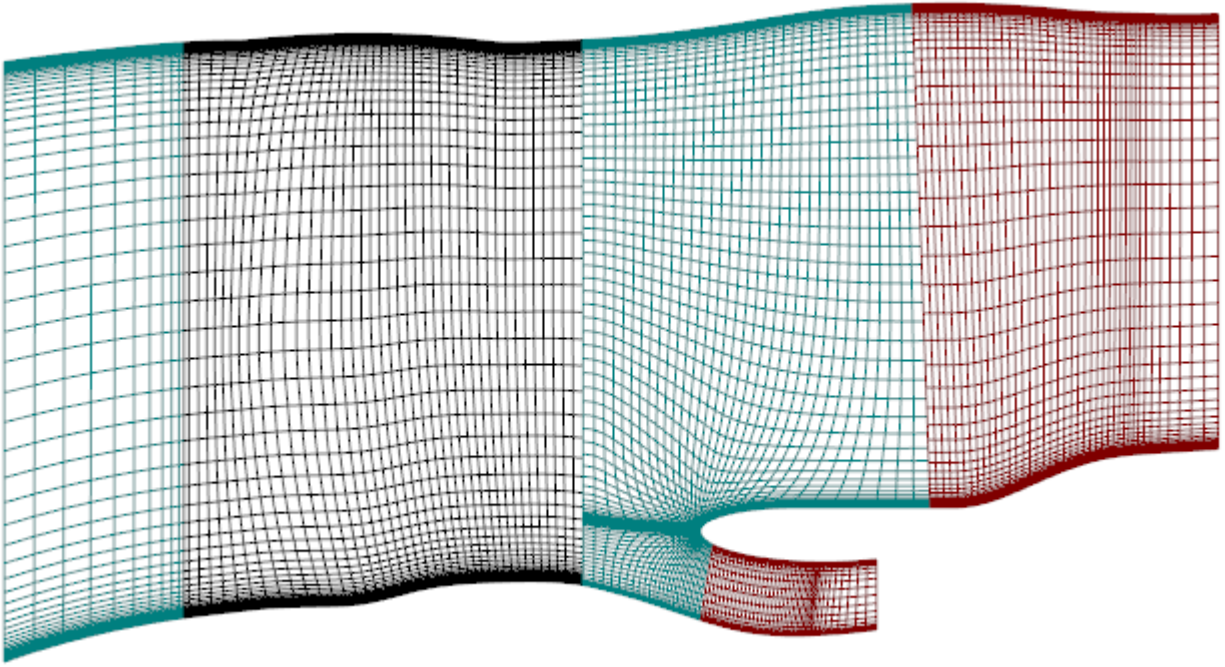
Figure 7: Meridional View of Three-Dimensional CFD Grid Blocks (Mid-Pitch Location)
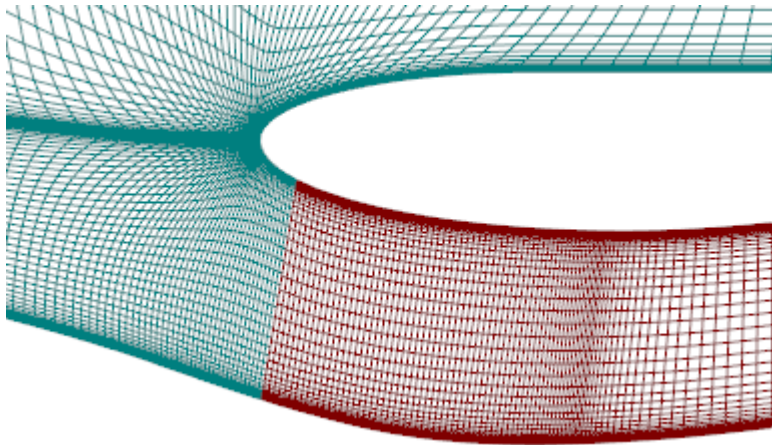
Figure 8: Enlarged Grid Blocks at Core Inlet Region
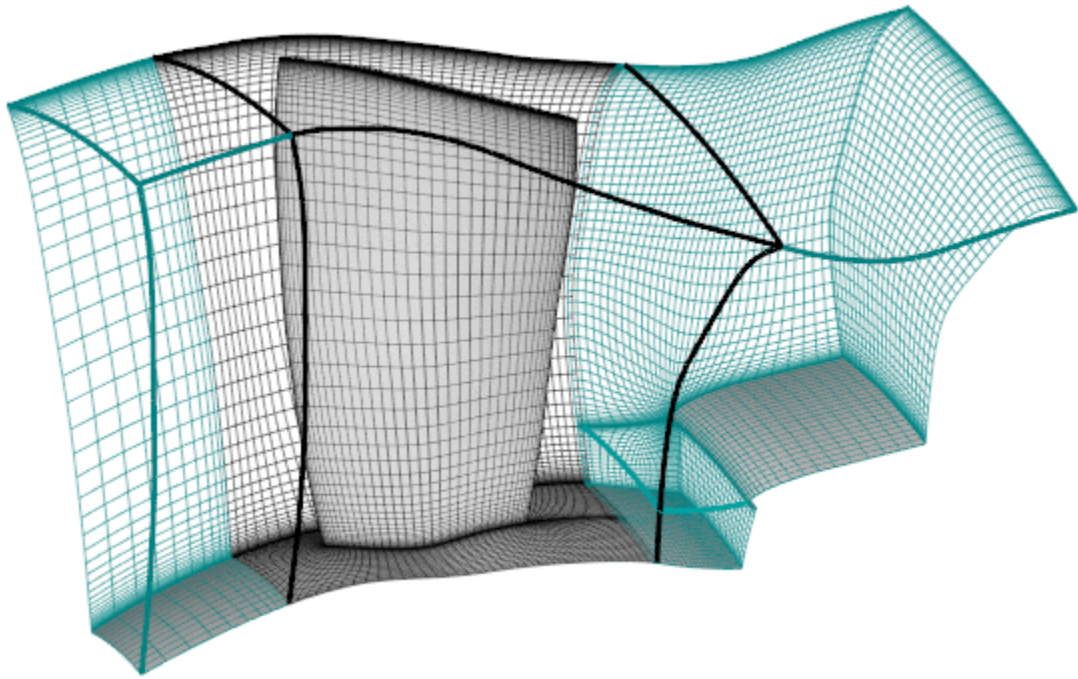
Figure 9: Three-Dimensional View of Rotor Grid
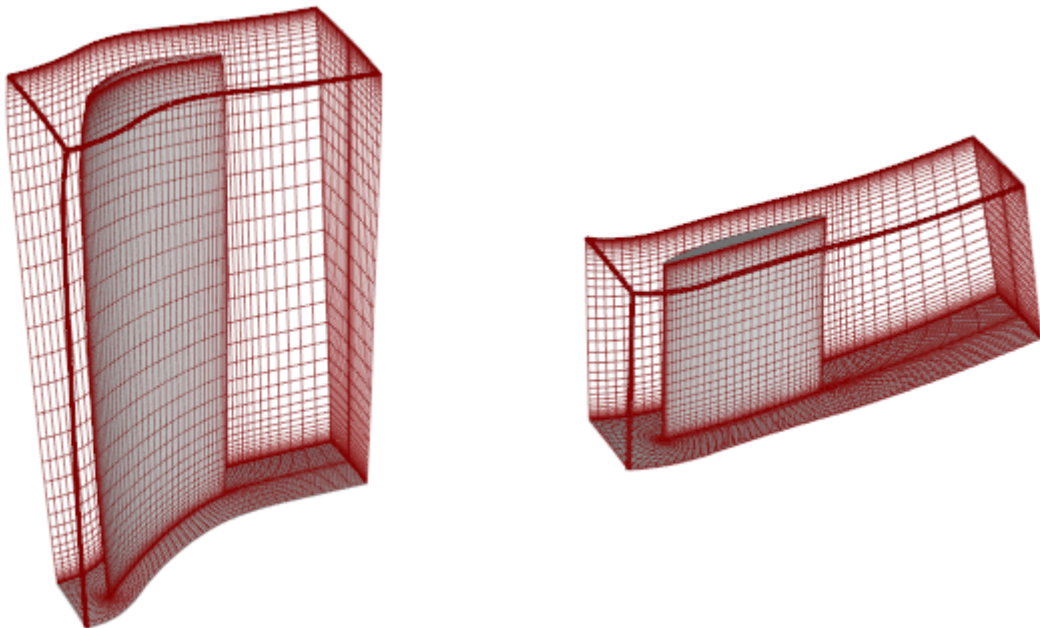
Figure 10: Three-Dimensional View of FEGV Grid (left) and CIGV Grid (right)

Rotor Near Tip

Rotor Near Mid

Rotor Near Hub
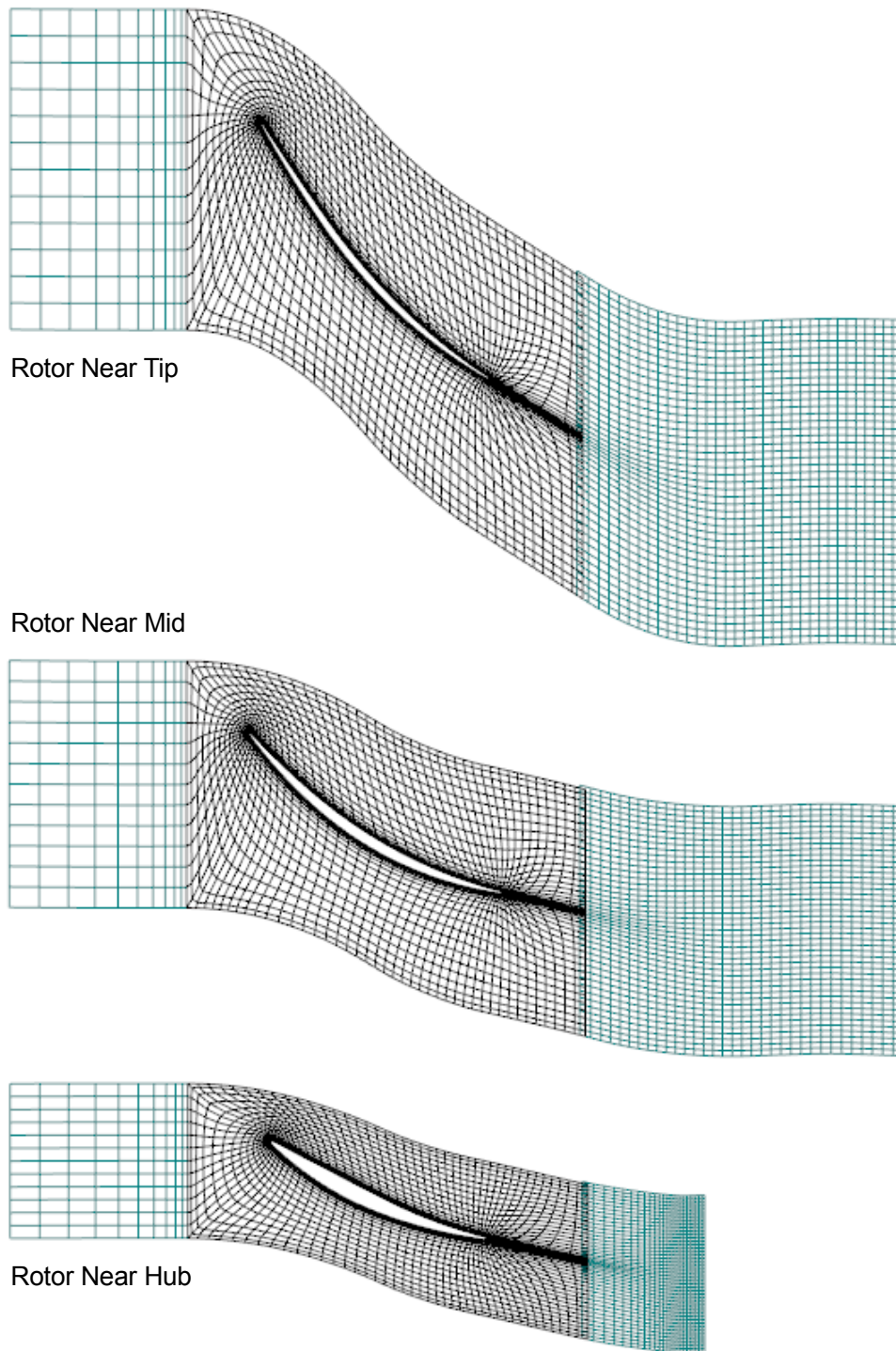
Figure 11: Rotor Grid at Three Spanwise Locations
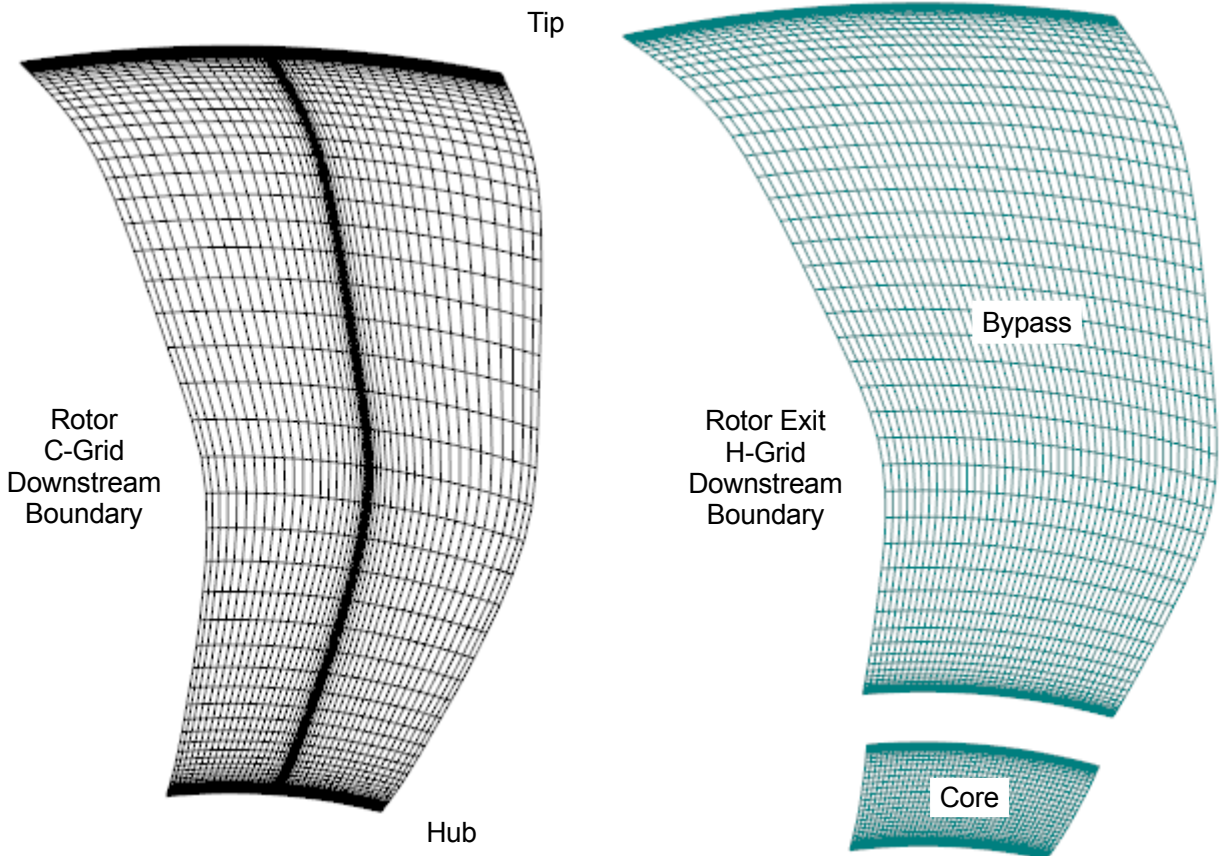
Figure 12: Rotor Grid at Block Downstream Boundaries
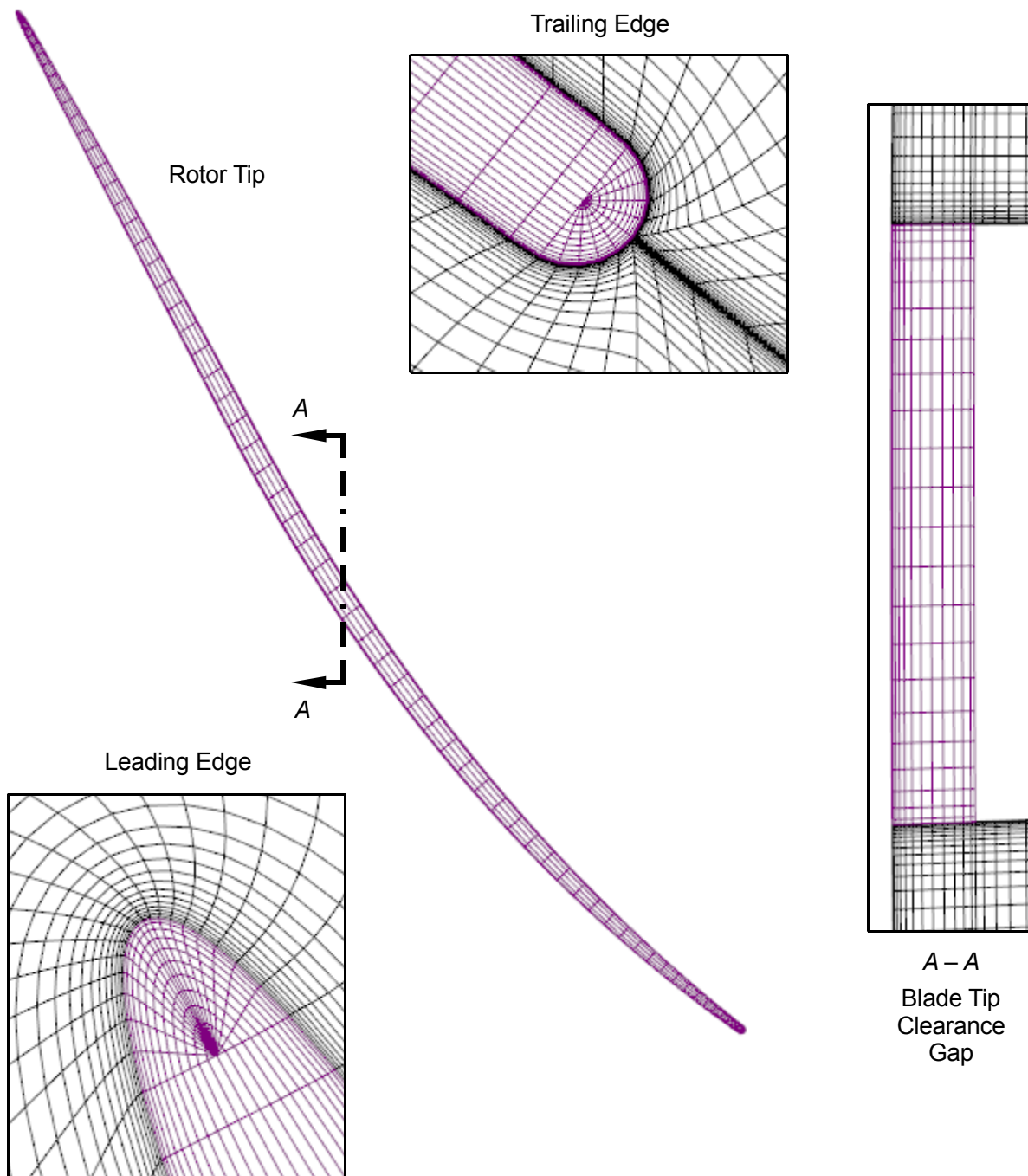
Figure 13: Rotor Tip Clearance Grid

Trailing Clearance

Rotor Hub

Hub Trunnion
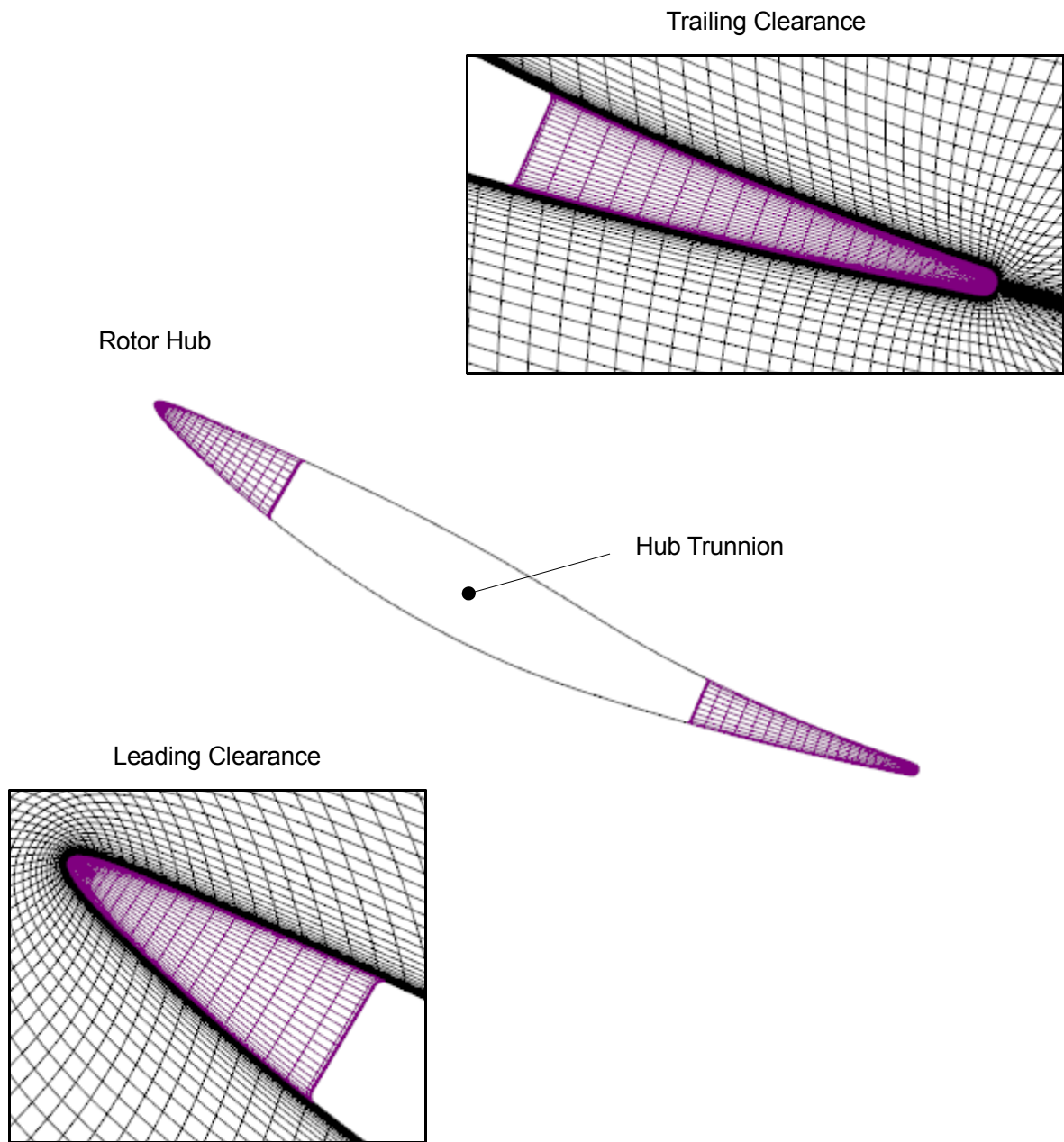
Leading Clearance

Figure 14: Rotor Hub Clearance Grid

FEGV Near Midspan
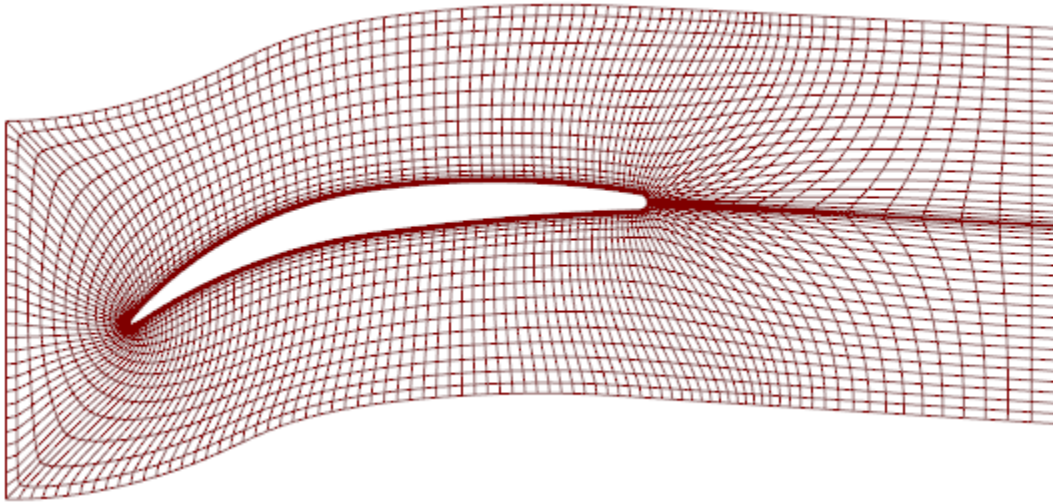
Leading Edge
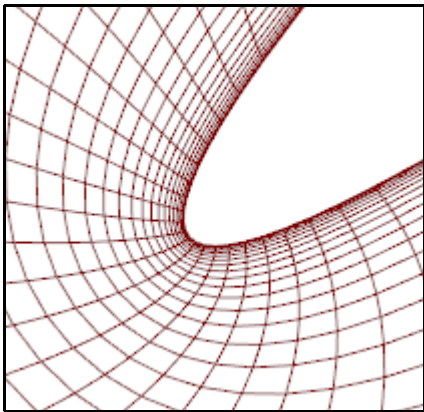
Trailing Edge
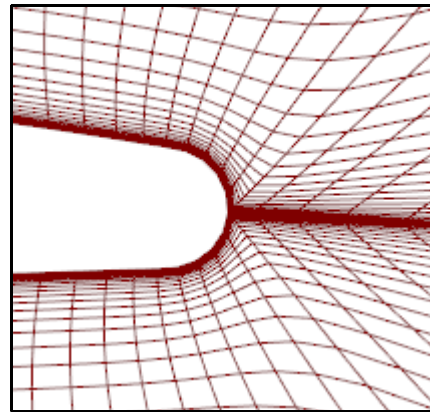
Figure 15: FEGV Grid at Near Midspan Location

FEGV C-Grid
Downstream
Boundary

Tip

Hub
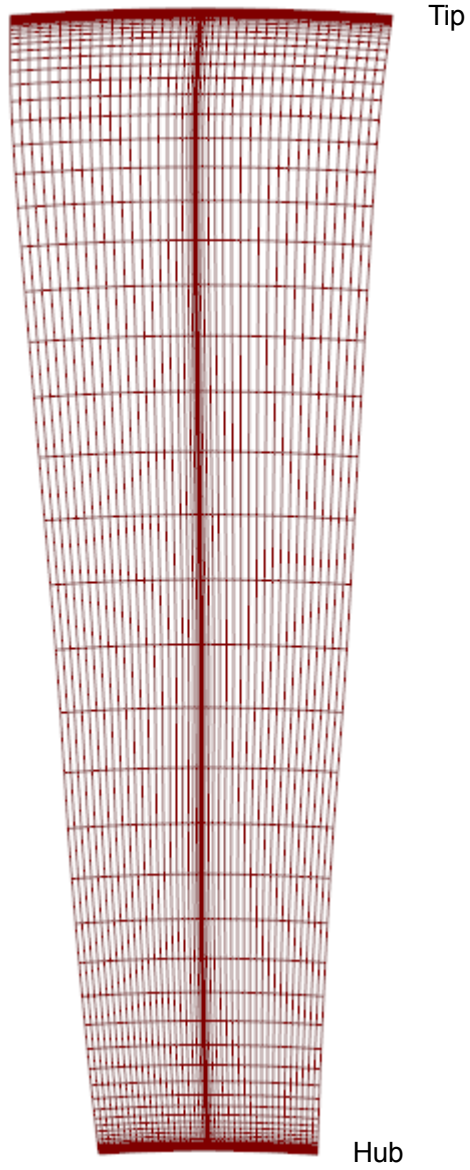
Figure 16: FEGV Grid at Block Downstream Boundary

CIGV Near Midspan
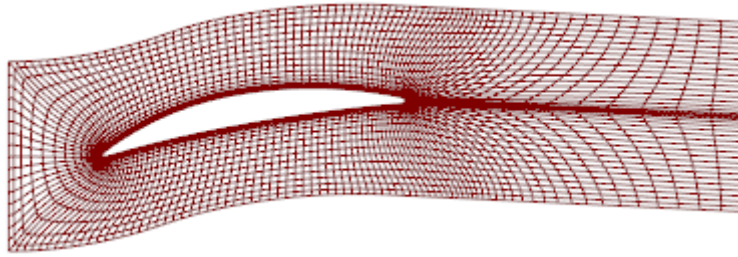
CIGV C-Grid
Downstream
Boundary

Tip

Hub
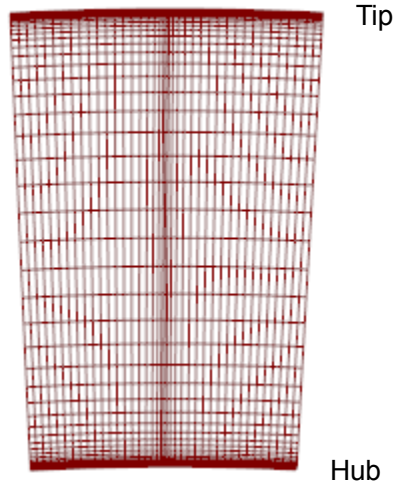
Figure 17: CIGV Grid at Near Midspan Location and at Block Downstream Boundary
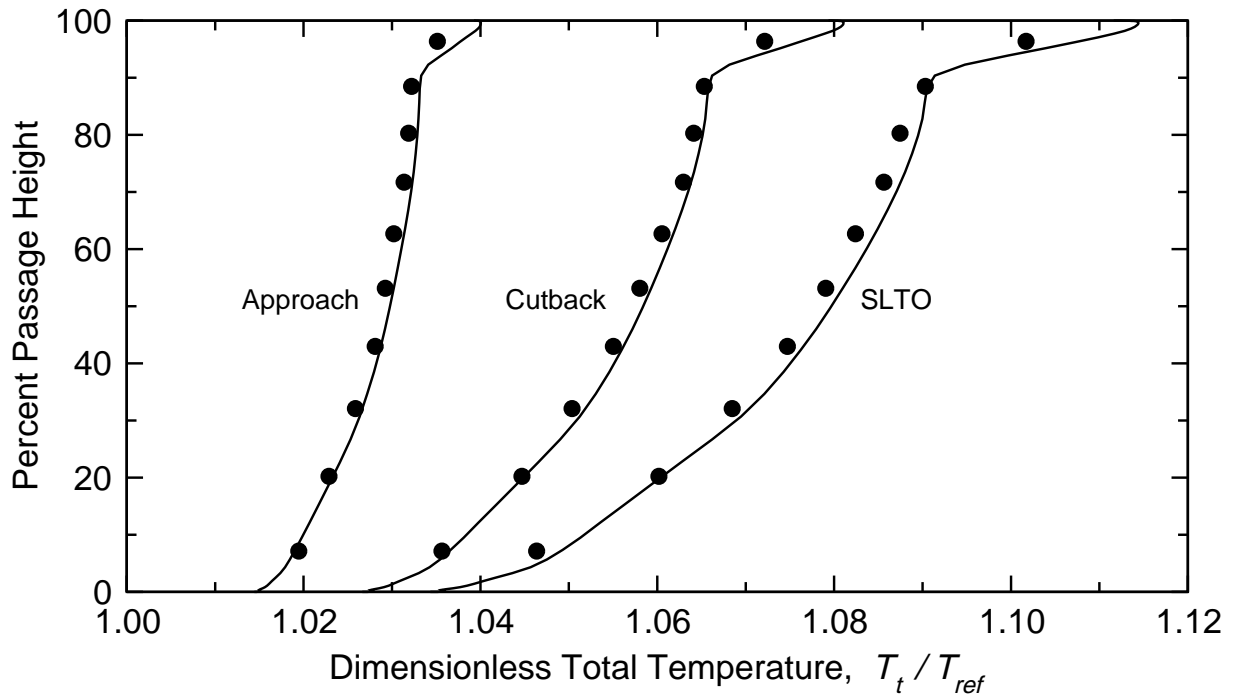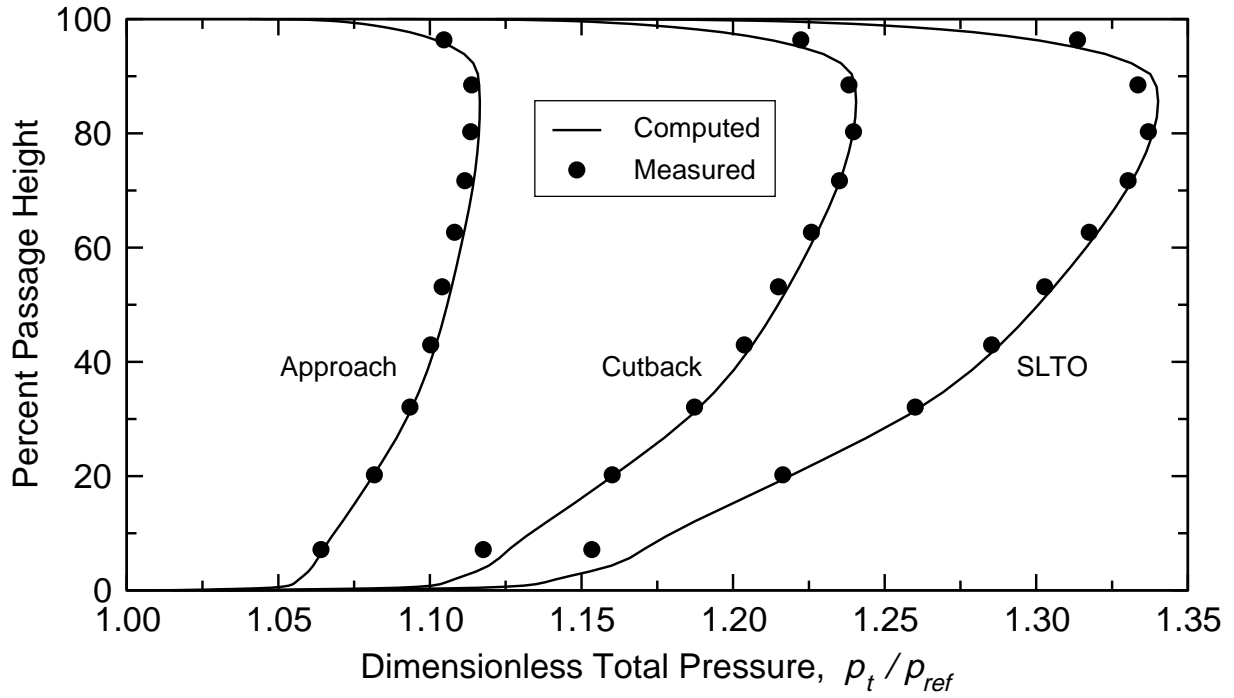
Figure 18: Computed and Measured Rotor Exit Total-Pressure and Total-Temperature Spanwise Distributions in the Bypass Duct , Upstream of FEGV

SLTO Operating Point
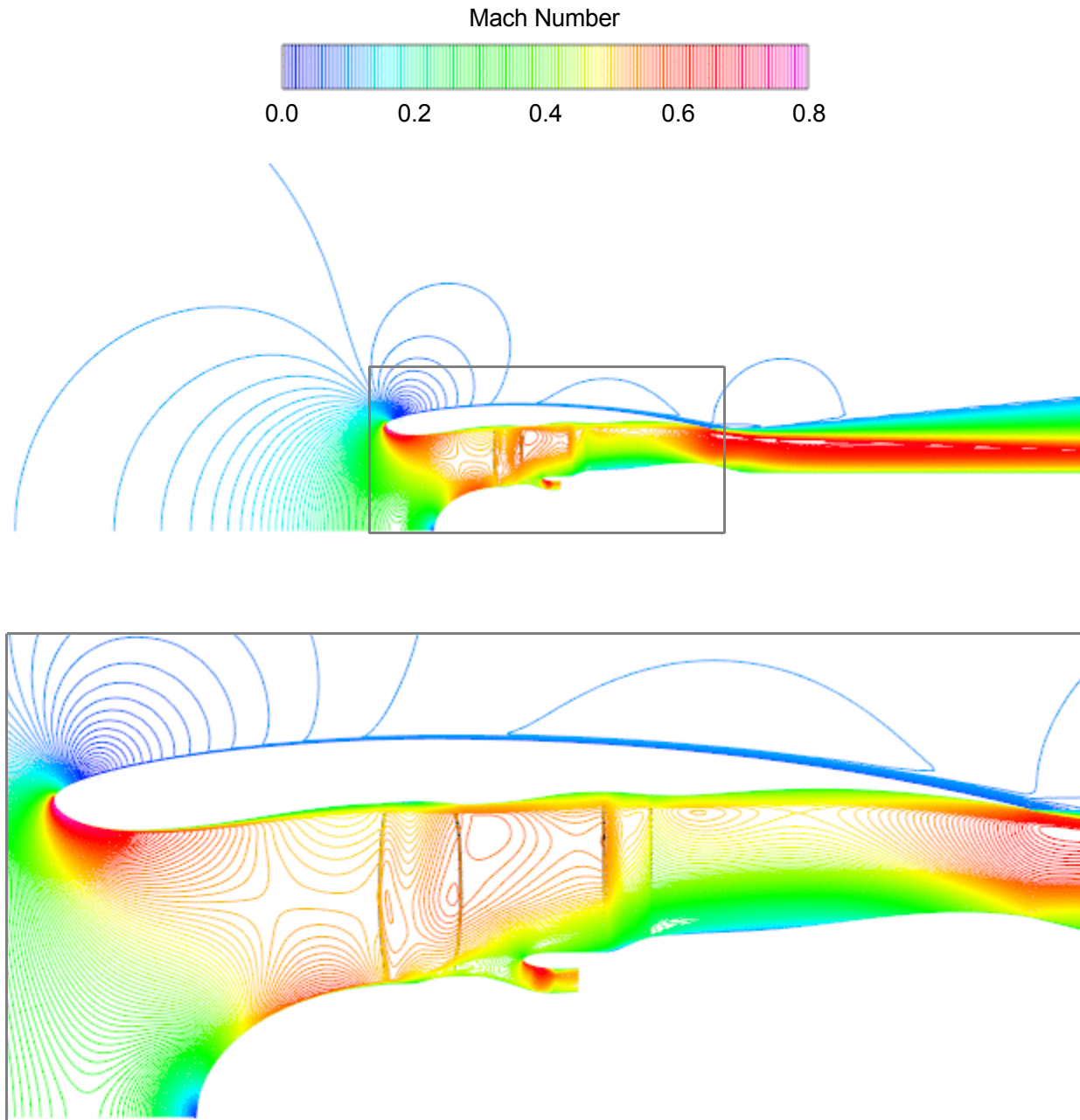
*Figure 19: Computed Fan System Flow Field for the SLTO Operating Point;
Pitchwise-Averaged Flow; Mach Number Contours*
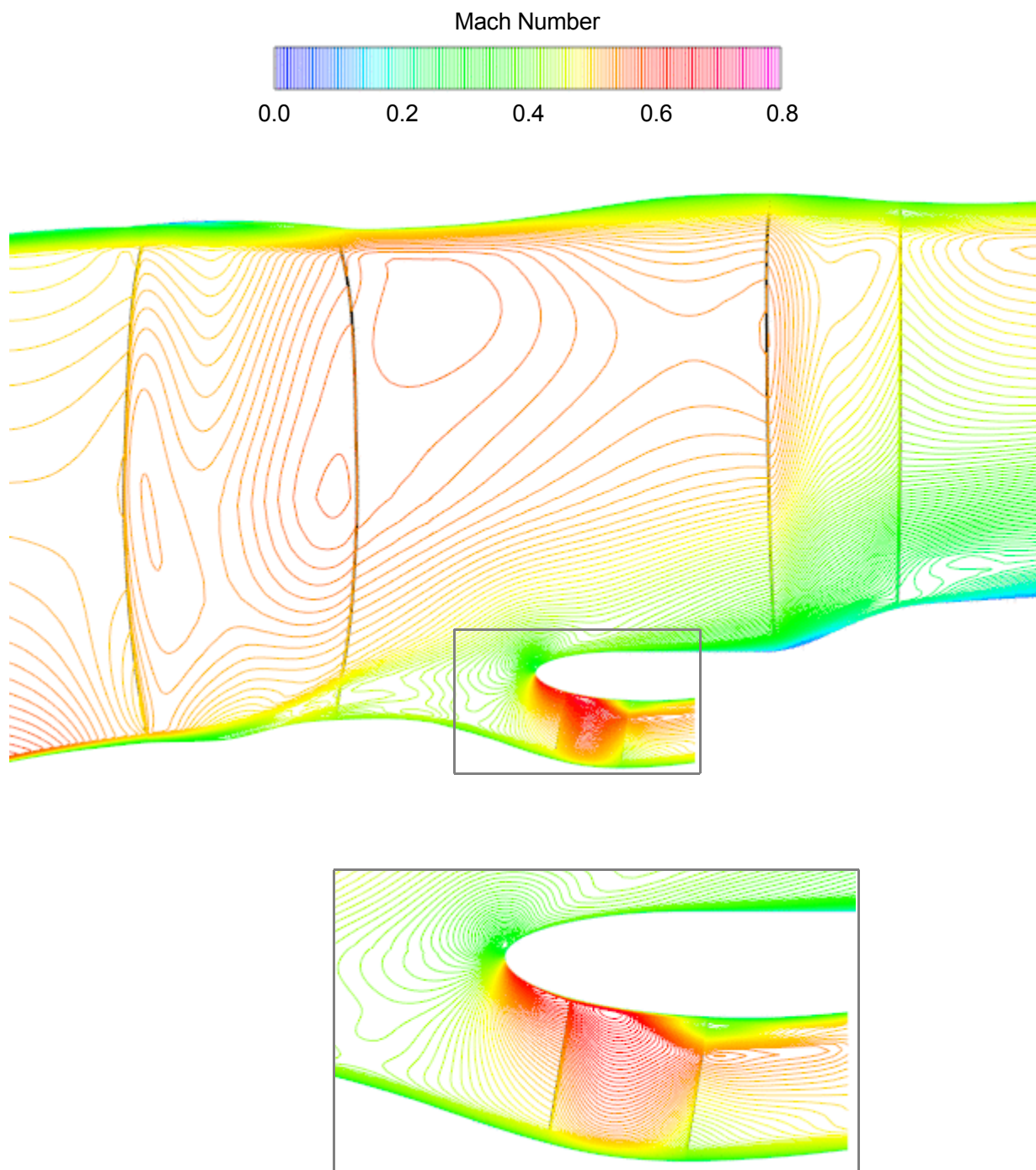
Figure 20: Computed Fan Blade Row Flow Fields for the SLTO Operating Point;
Pitchwise-Averaged Flow; Mach Number Contours

Turbulence Kinetic Energy

0.000   0.002   0.004   0.006   0.008
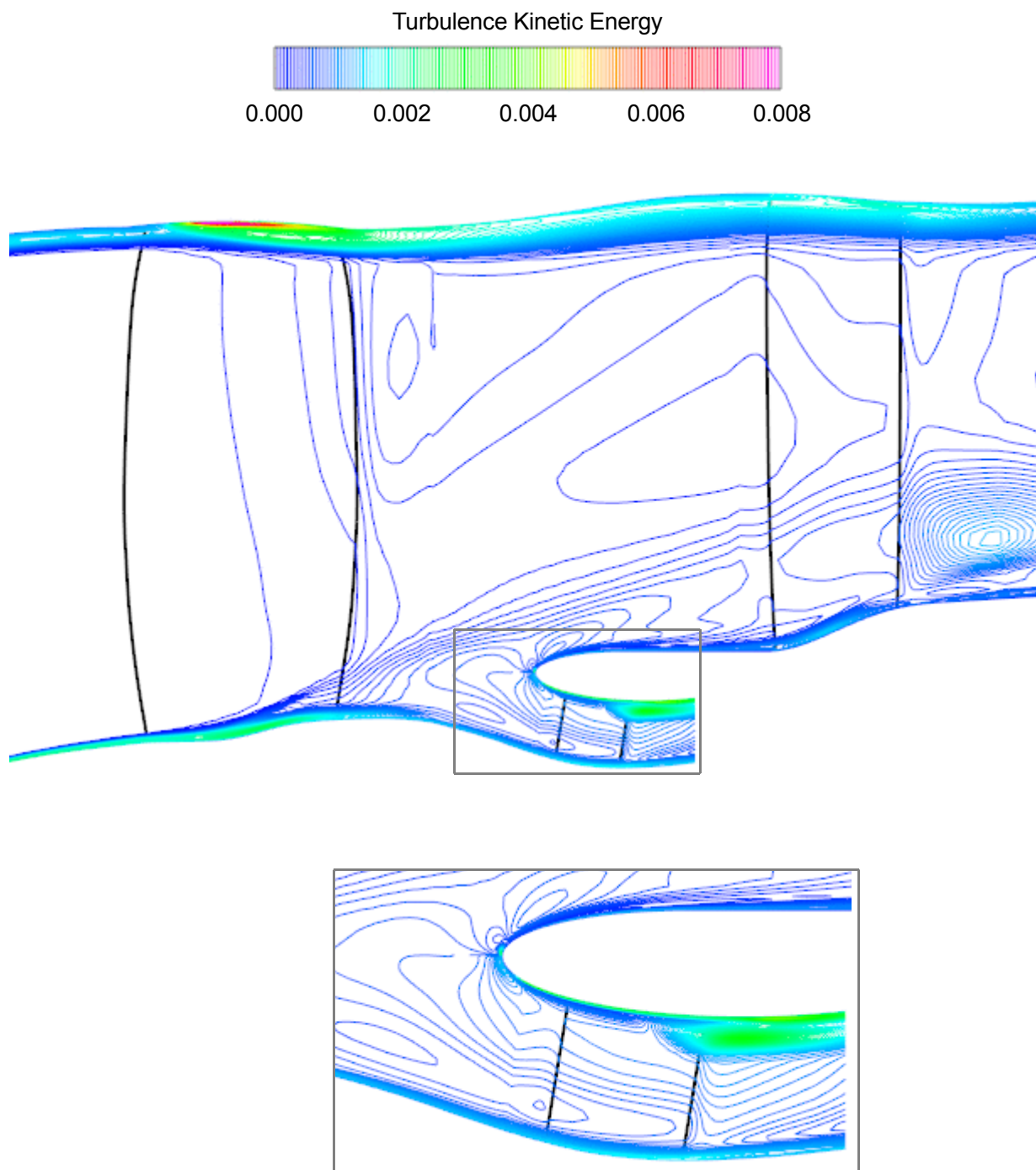
*Figure 21: Computed Fan Blade Row Flow Fields for the SLTO Operating Point;
Pitchwise-Averaged Flow; Turbulence Kinetic Energy Contours*

SLTO Operating Point
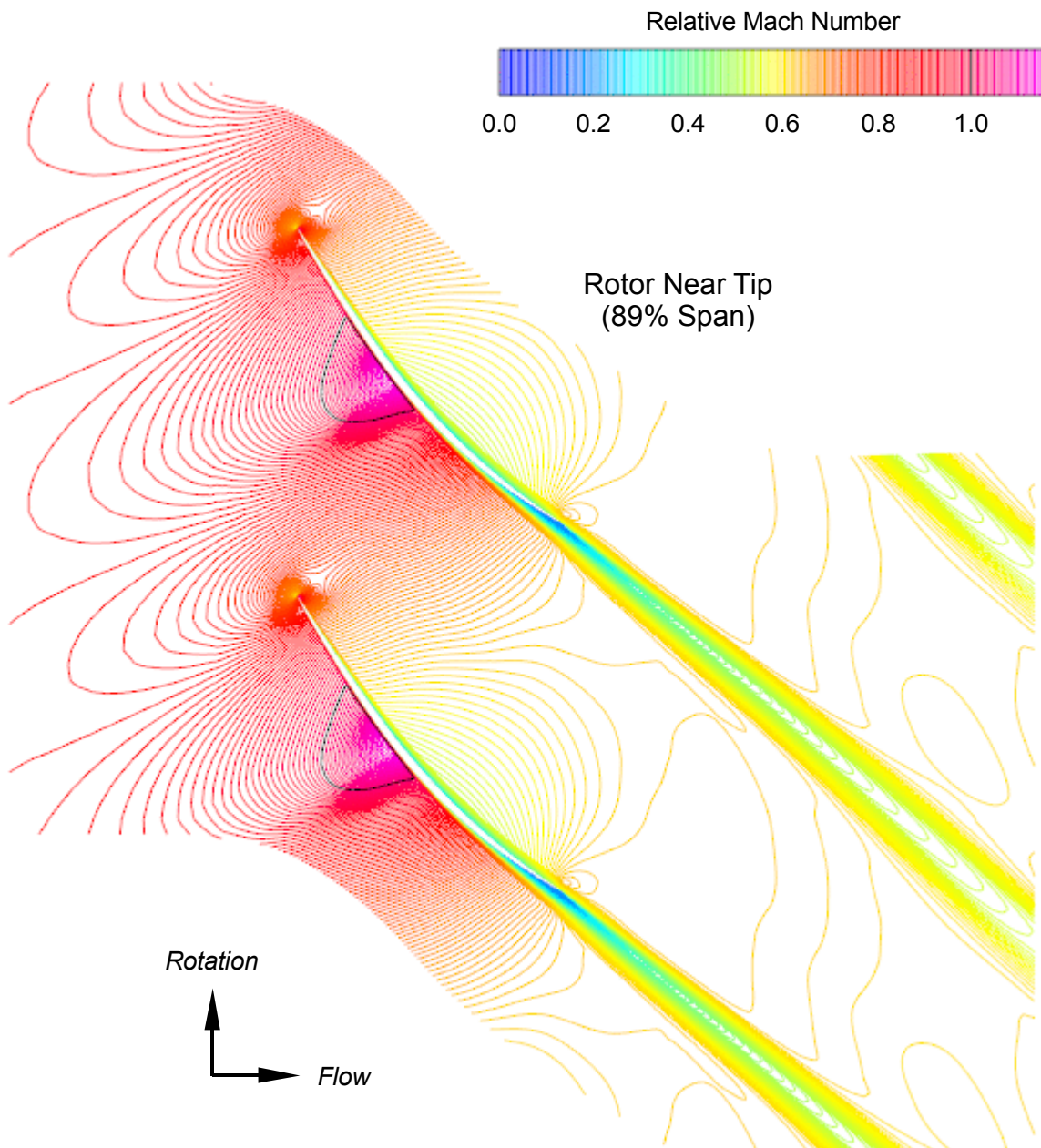
Figure 22a: Computed Rotor Flow Field for the SLTO Operating Point;
Blade-to-Blade Relative Mach Number Contours

Rotor Near Mid
(51% Span)

Rotor Near Hub
(8% Span)
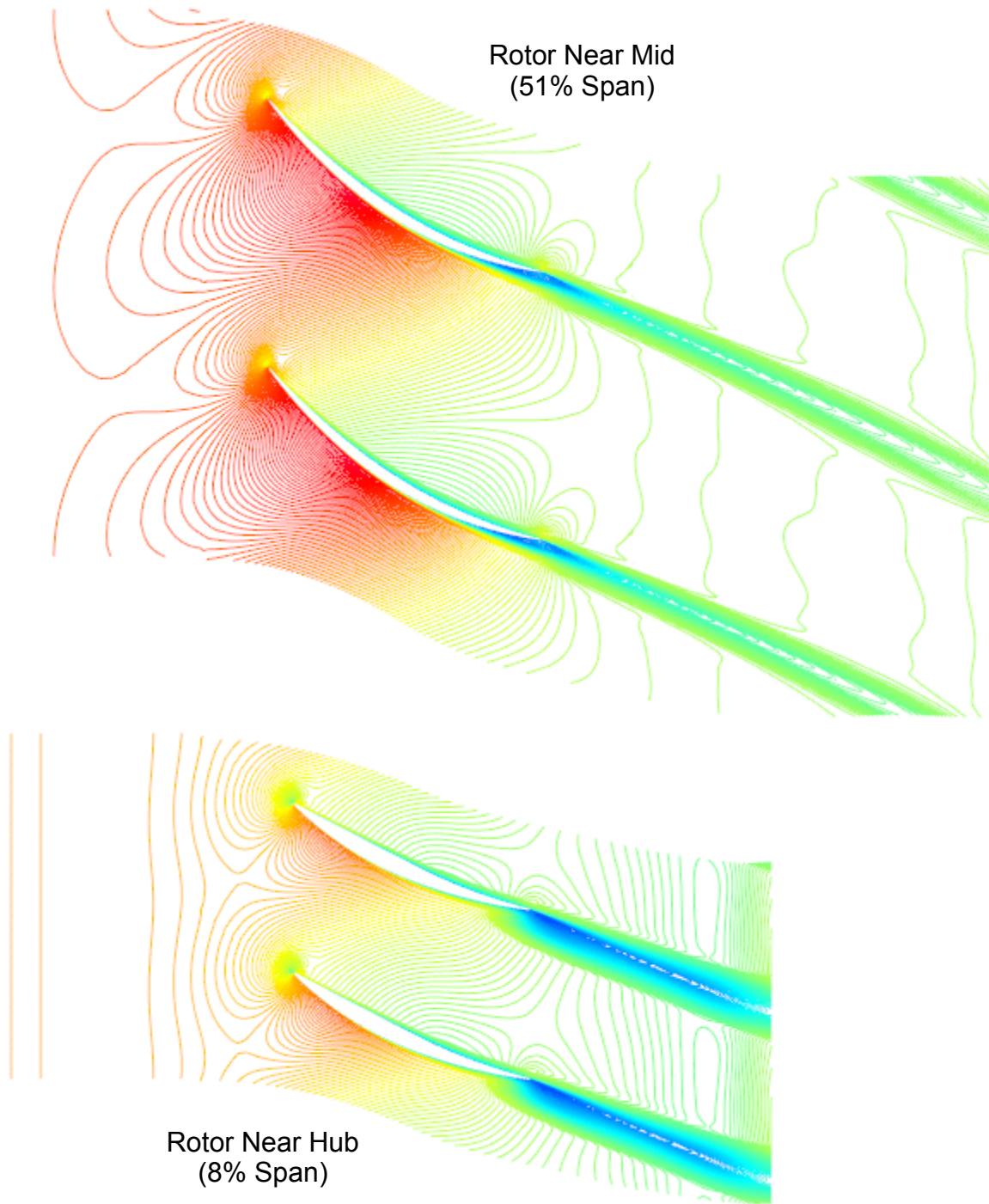
Figure 22b: Computed Rotor Flow Field for the SLTO Operating Point;
Blade-to-Blade Relative Mach Number Contours

Rotor Tip Clearance

Mid-Clearance-Gap
Spanwise Location

Mid-Chord
Axial Location

Rotation
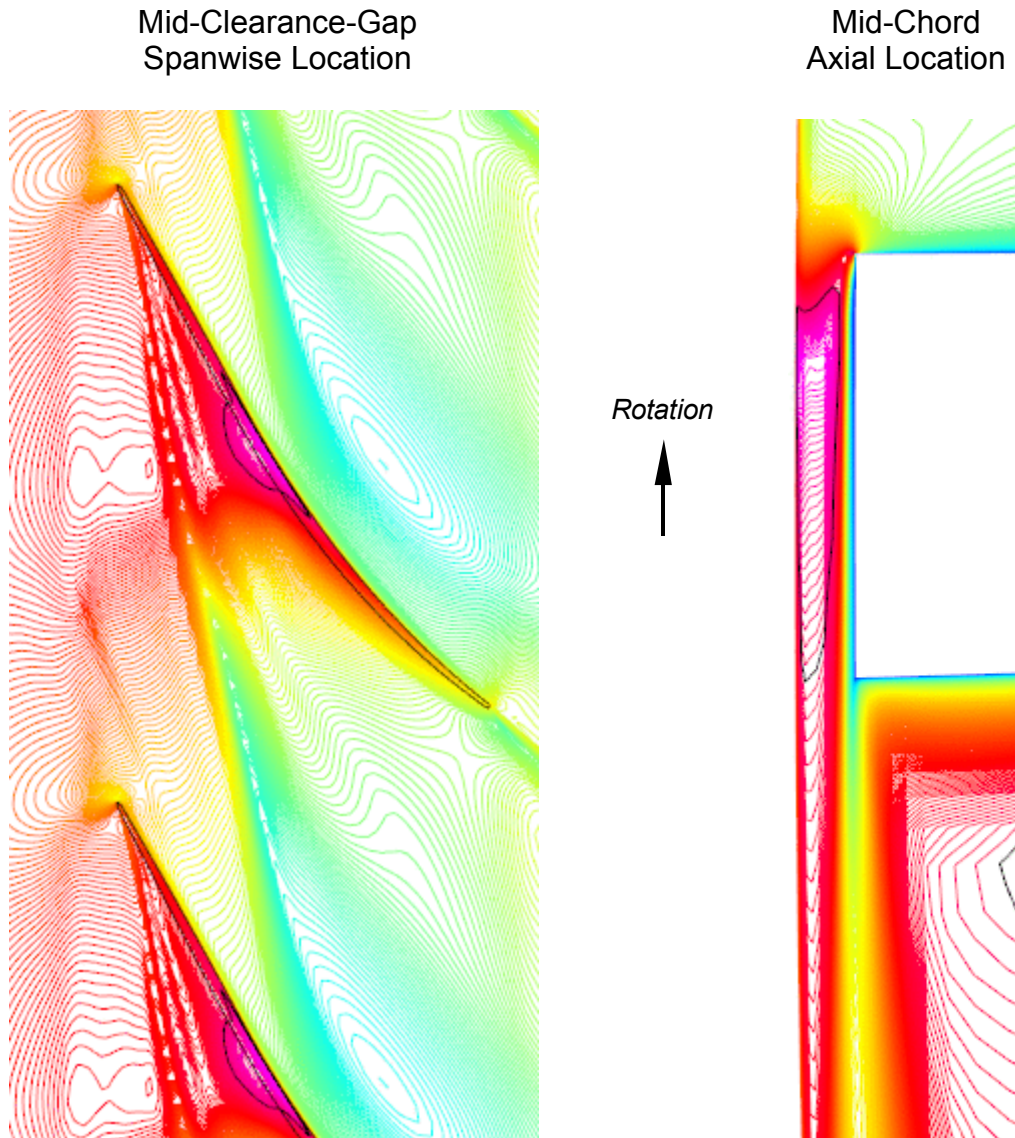
*Figure 23: Computed Rotor Tip Flow Field for the SLTO Operating Point;
Relative Mach Number Contours (Legend in Figure 22a)*

Rotor Hub Clearance

Mid-Clearance-Gap
Spanwise Location

Mid-Chord
Axial Location

Rotation
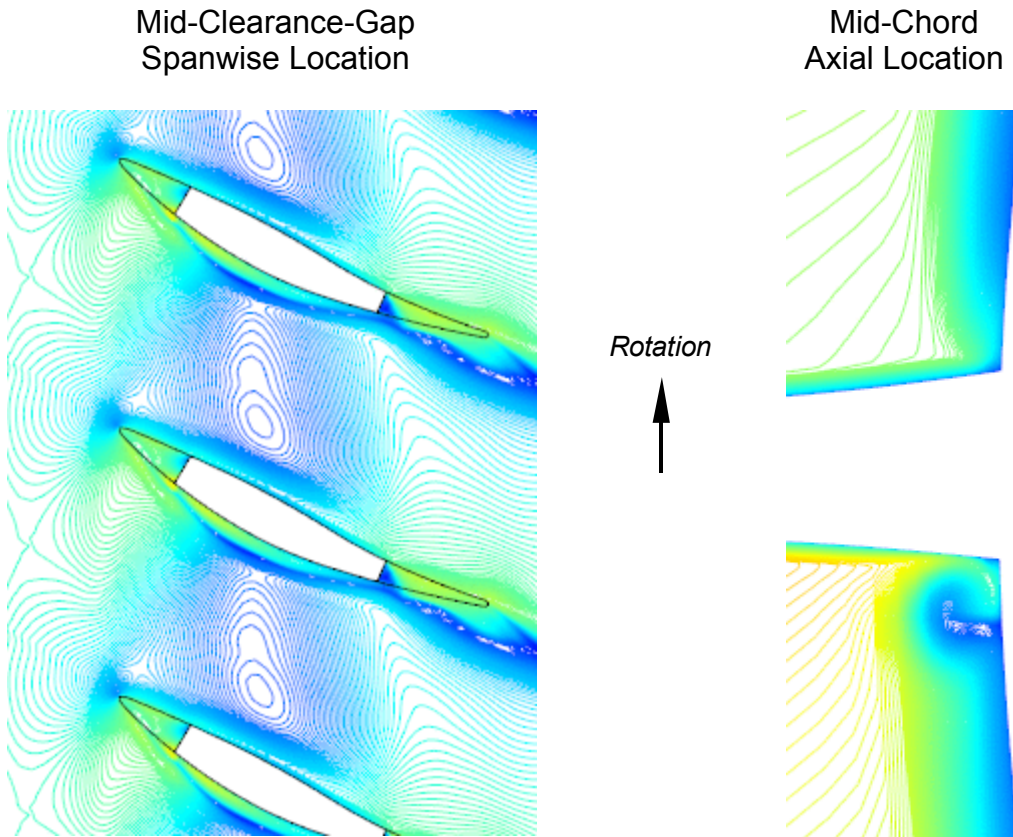
*Figure 24: Computed Rotor Hub Flow Field for the SLTO Operating Point;
Relative Mach Number Contours (Legend in Figure 22a)*

Figure 25: Computed Rotor Flow Field for the SLTO Operating Point; Downstream Boundary of C-Grid; Relative Mach Number Contours
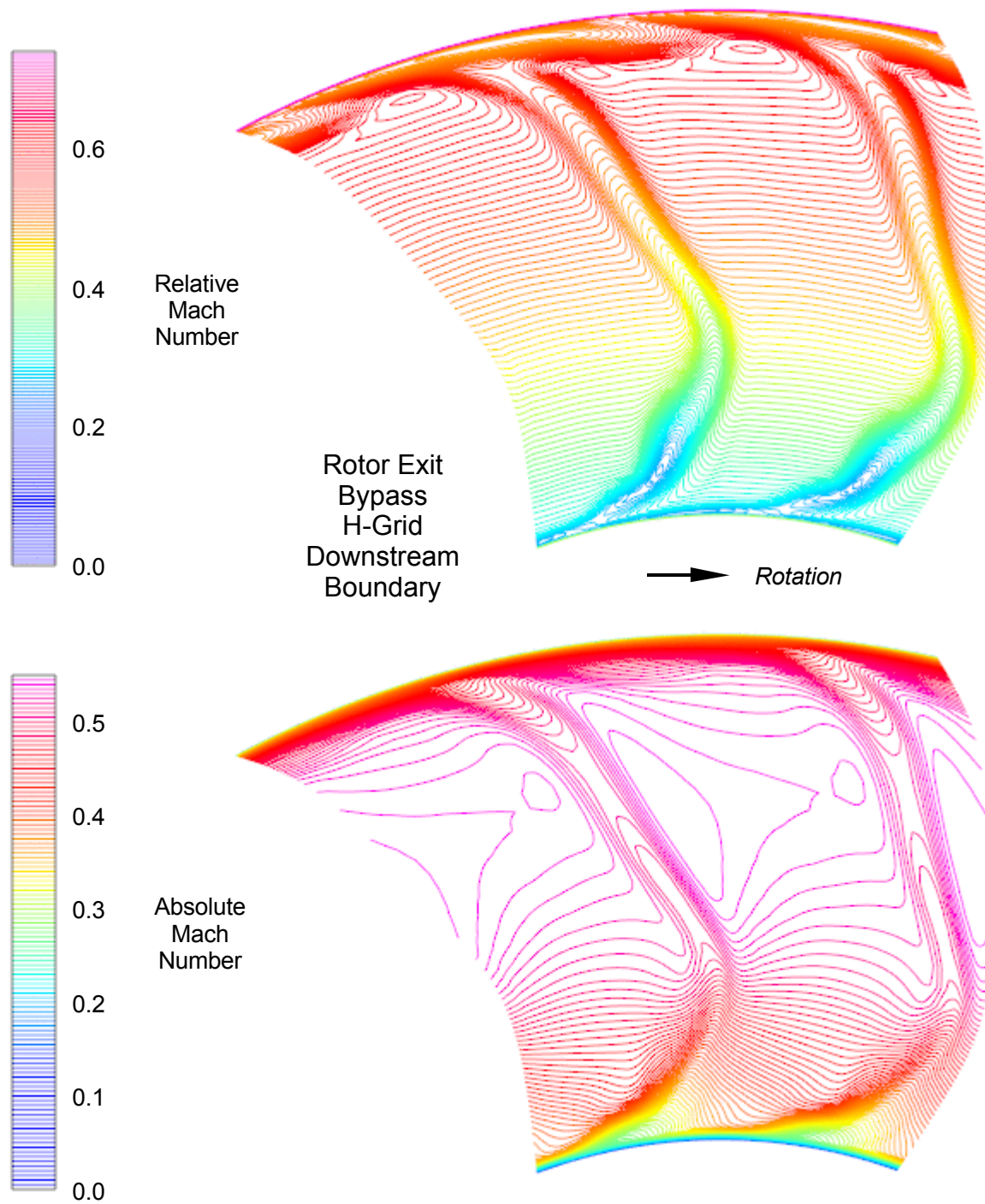
Figure 26a: Computed Rotor Flow Field for the SLTO Operating Point; Downstream Mixing Plane; Relative and Absolute Mach Number Contours
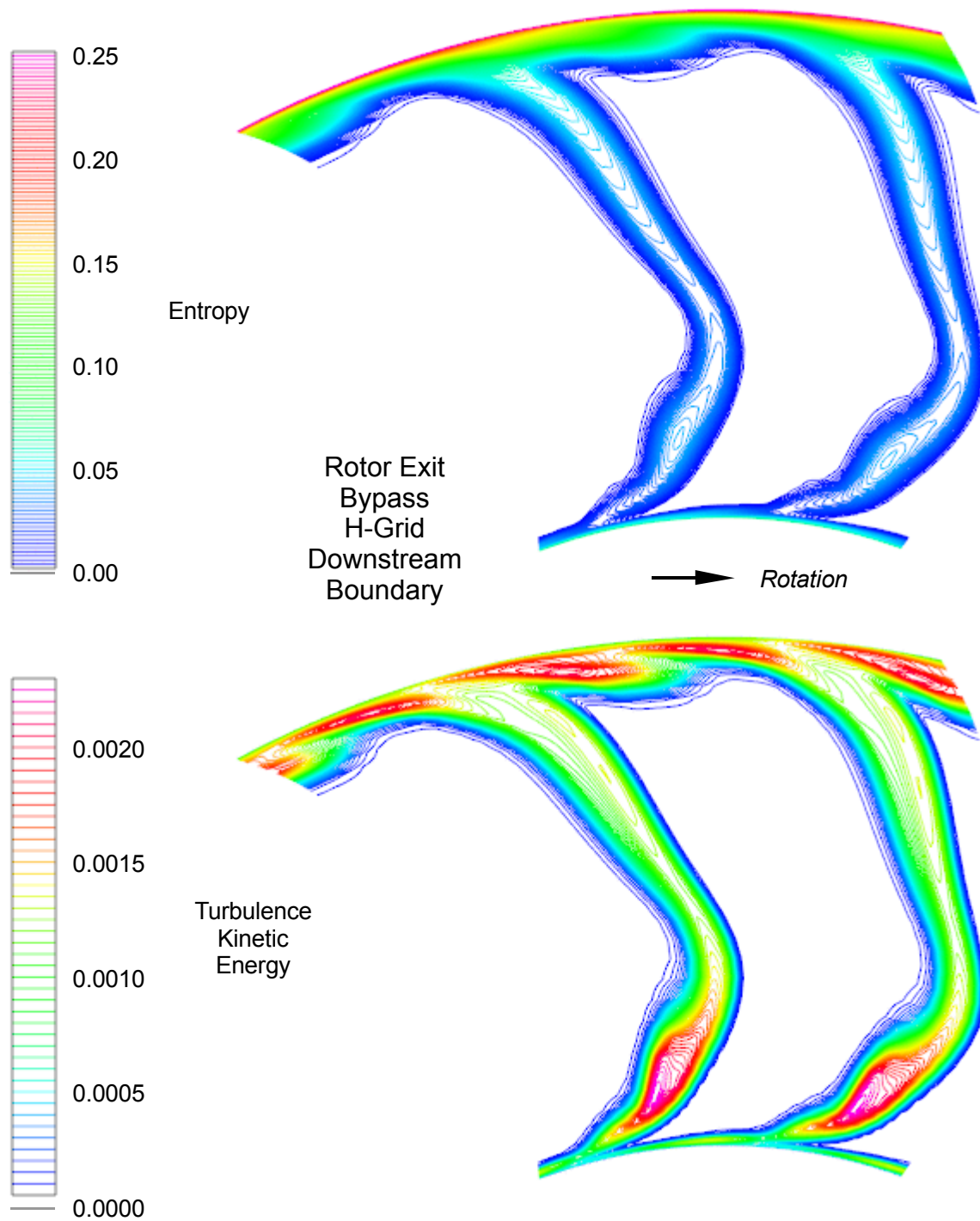
Figure 26b: Computed Rotor Flow Field for the SLTO Operating Point; Downstream Mixing Plane; Entropy and Turbulence Kinetic Energy Contours

SLTO Operating Point

Mach Number

0.0   0.2   0.4   0.6   0.8

FEGV Near Tip
(89% Span)
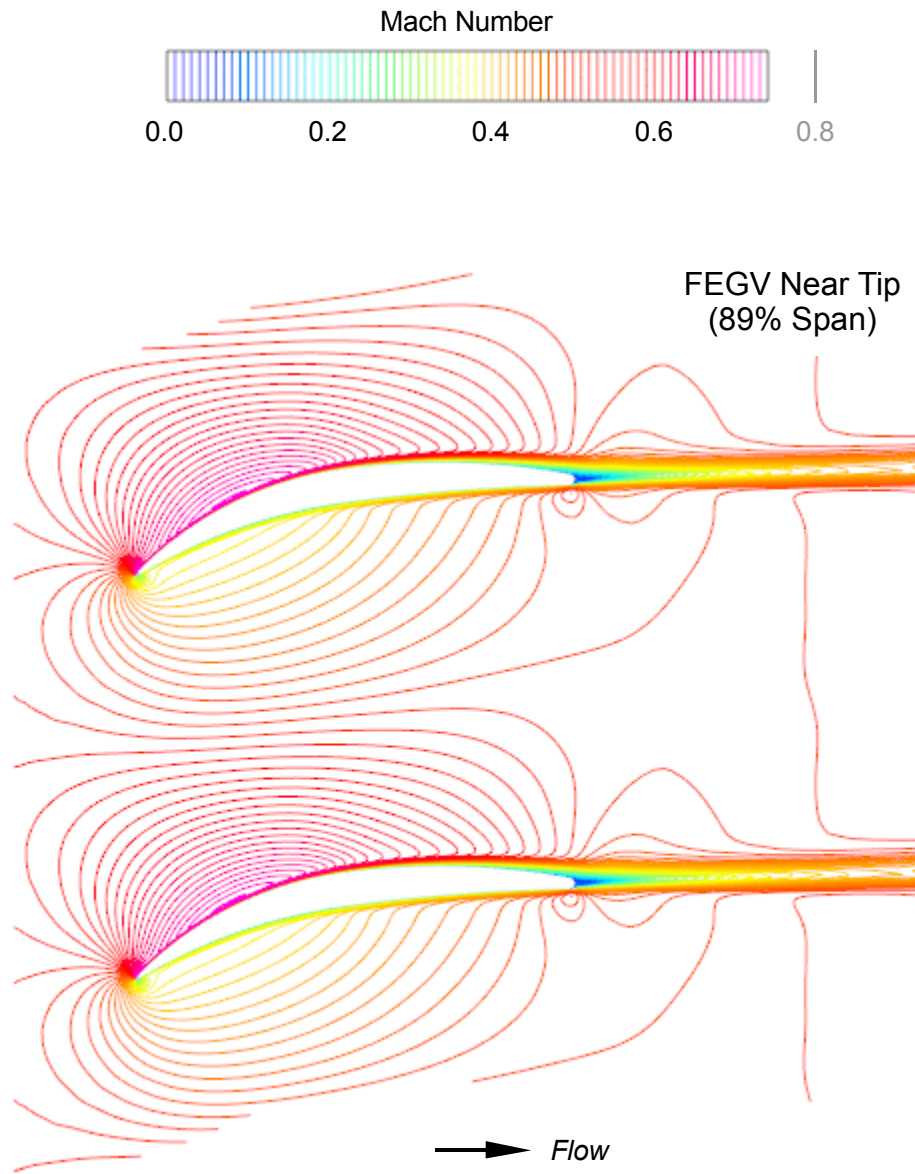
Flow

*Figure 27a: Computed FEGV Flow Field for the SLTO Operating Point;
Blade-to-Blade Mach Number Contours*

FEGV Near Mid
(48% Span)

→ *Flow*

FEGV Near Hub
(10% Span)
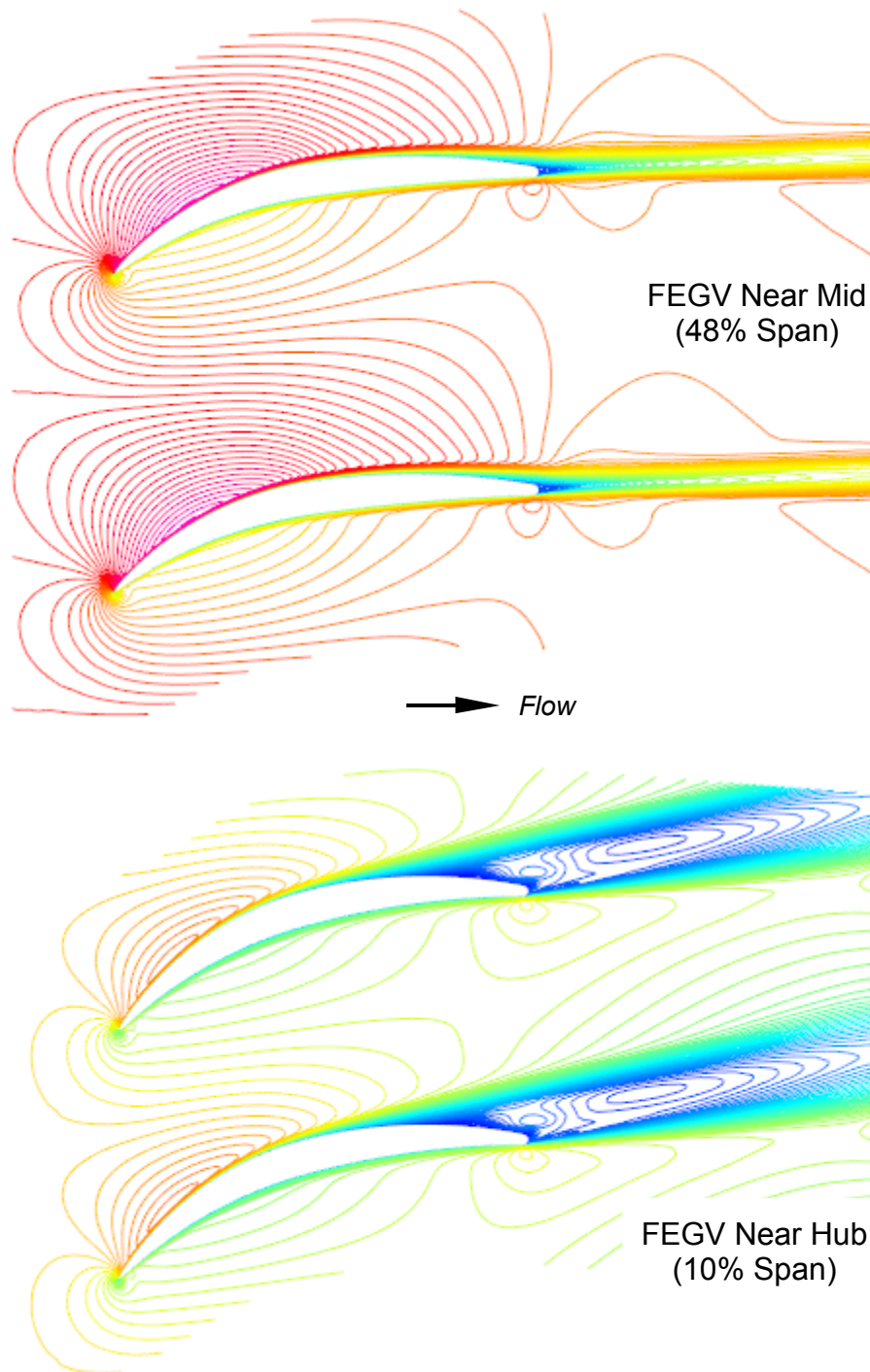
*Figure 27b: Computed FEGV Flow Field for the SLTO Operating Point;
Blade-to-Blade Mach Number Contours*

FEGV C-Grid
Downstream
Boundary

Mach
Number

0.5

0.4

0.3

0.2

0.1

0.0
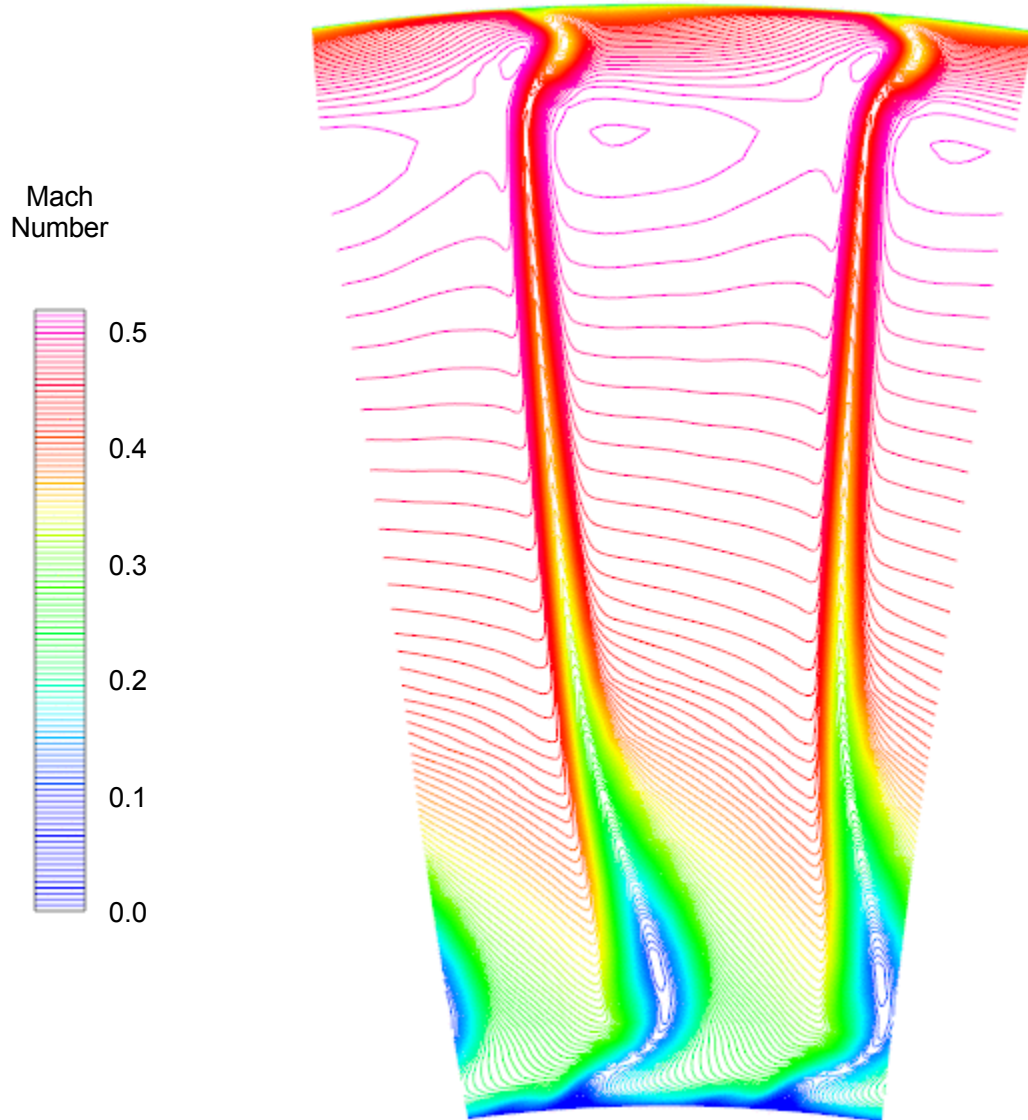
Figure 28: Computed FEGV Flow Field for the SLTO Operating Point;
Downstream Mixing Plane; Mach Number Contours

Cutback Operating Point
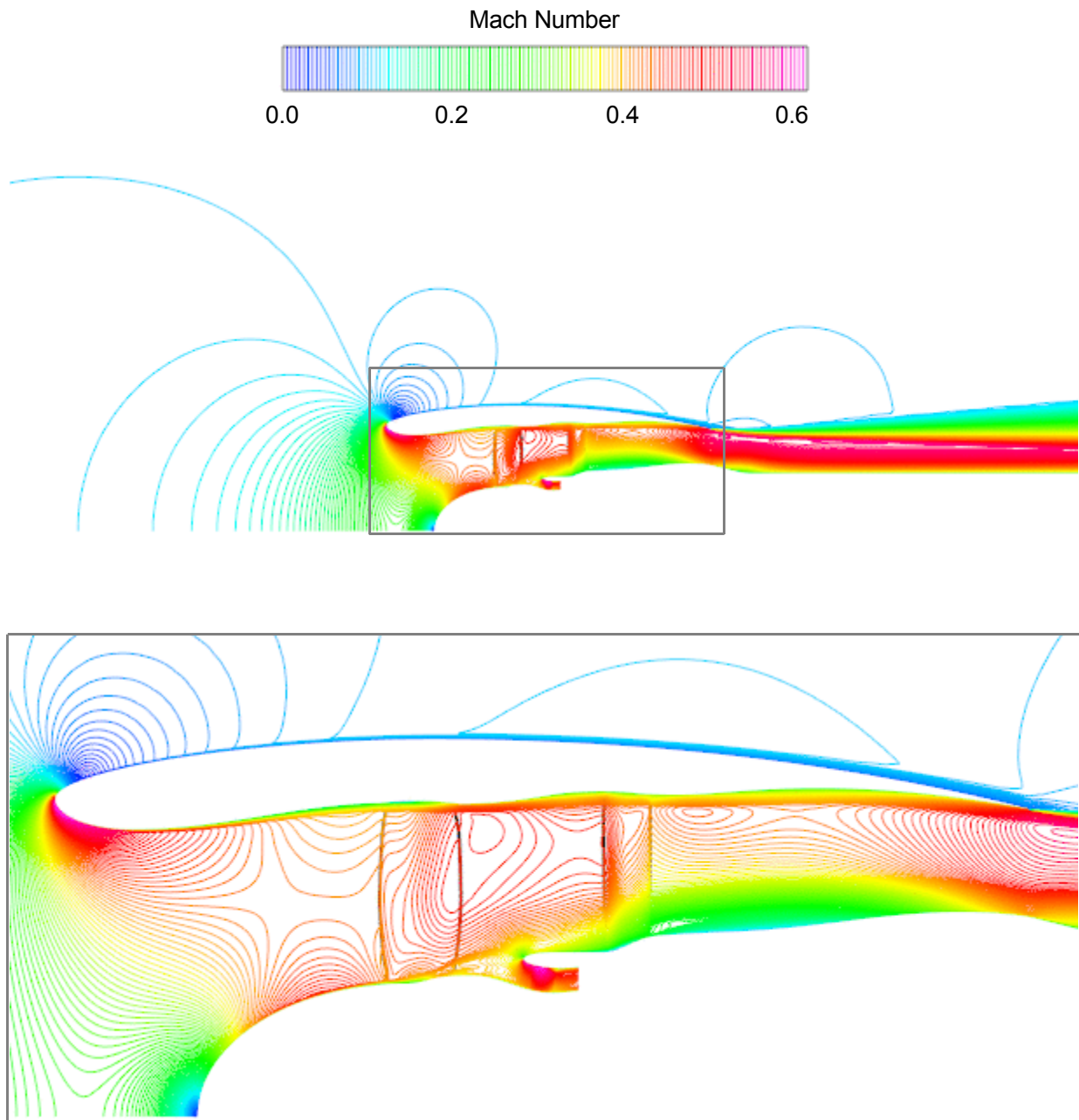
Figure 29: Computed Fan System Flow Field for the Cutback Operating Point;
Pitchwise-Averaged Flow; Mach Number Contours
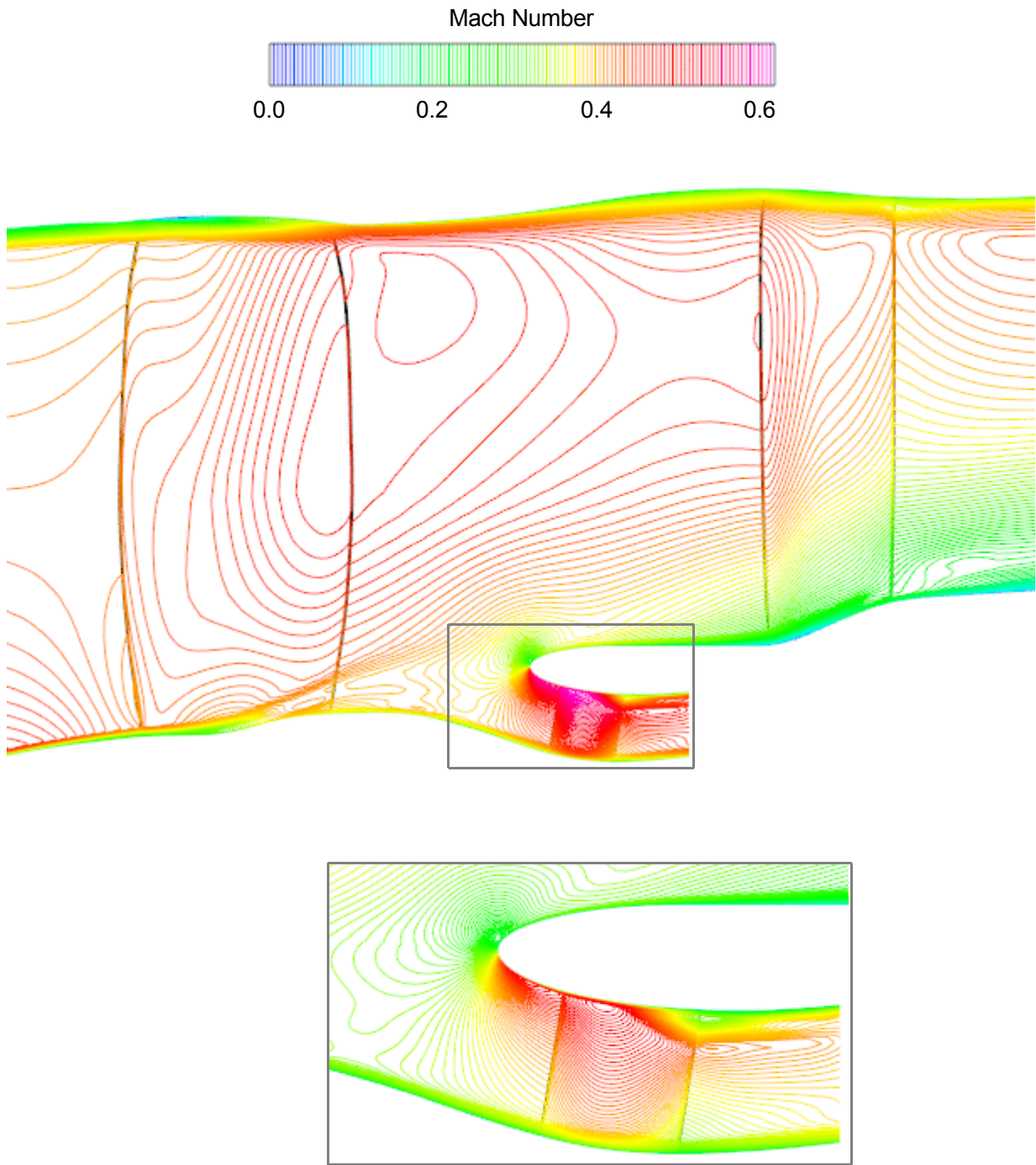
Figure 30: Computed Fan Blade Row Flow Fields for the Cutback Operating Point; Pitchwise-Averaged Flow; Mach Number Contours

Cutback Operating Point
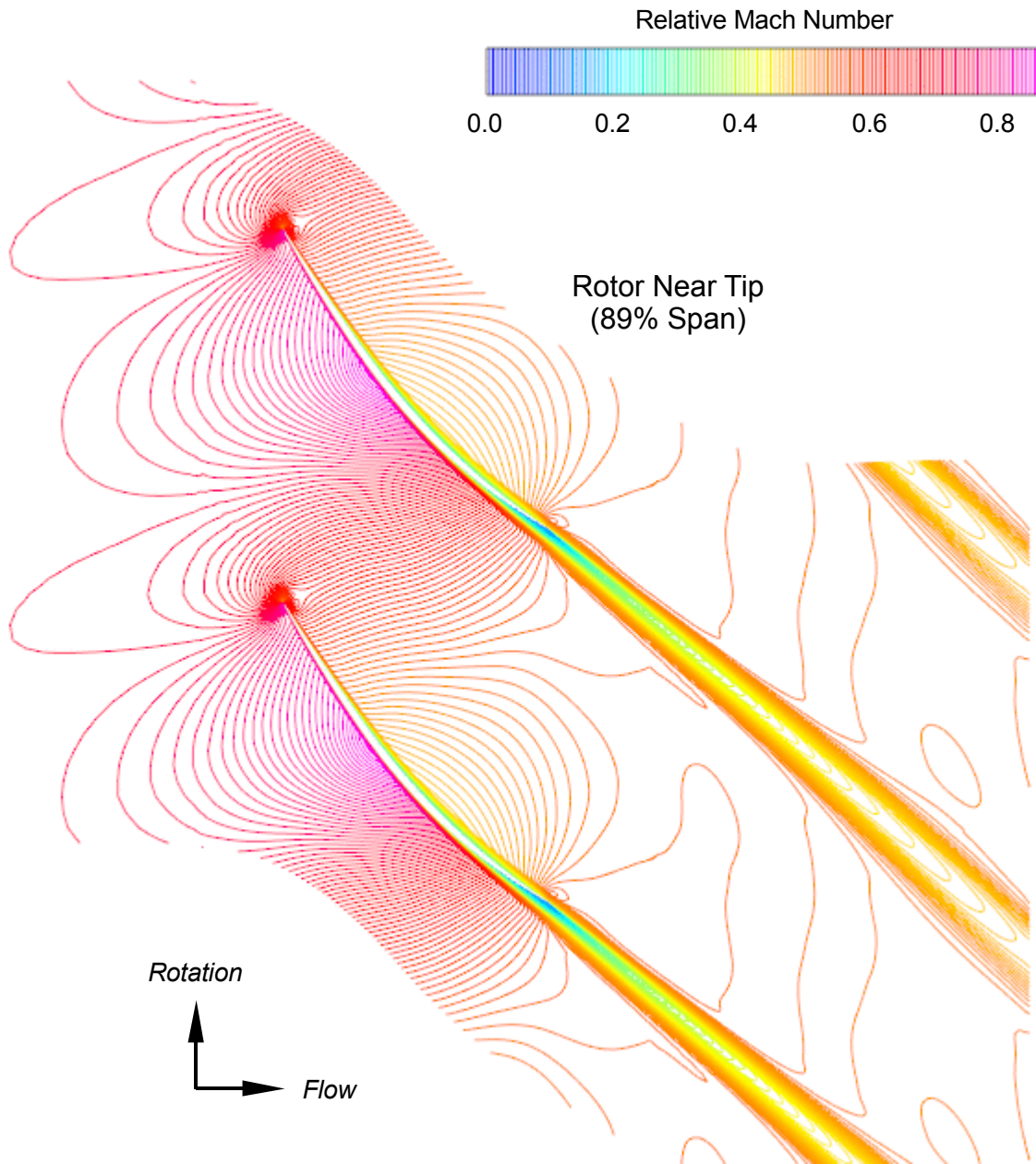
*Figure 31a: Computed Rotor Flow Field for the Cutback Operating Point;
Blade-to-Blade Relative Mach Number Contours*

Rotor Near Mid
(51% Span)

Rotor Near Hub
(8% Span)
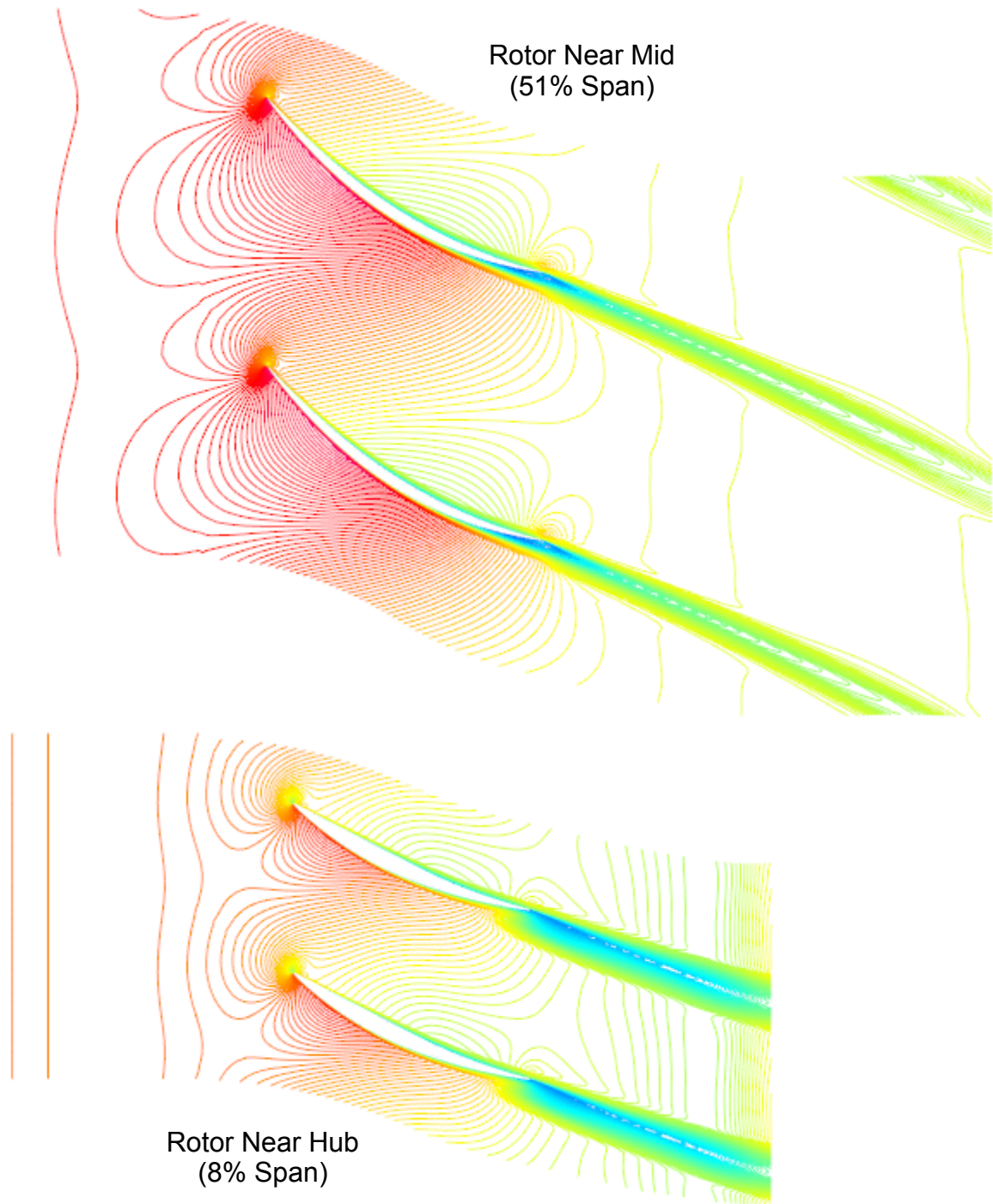
Figure 31b: Computed Rotor Flow Field for the Cutback Operating Point;
Blade-to-Blade Relative Mach Number Contours
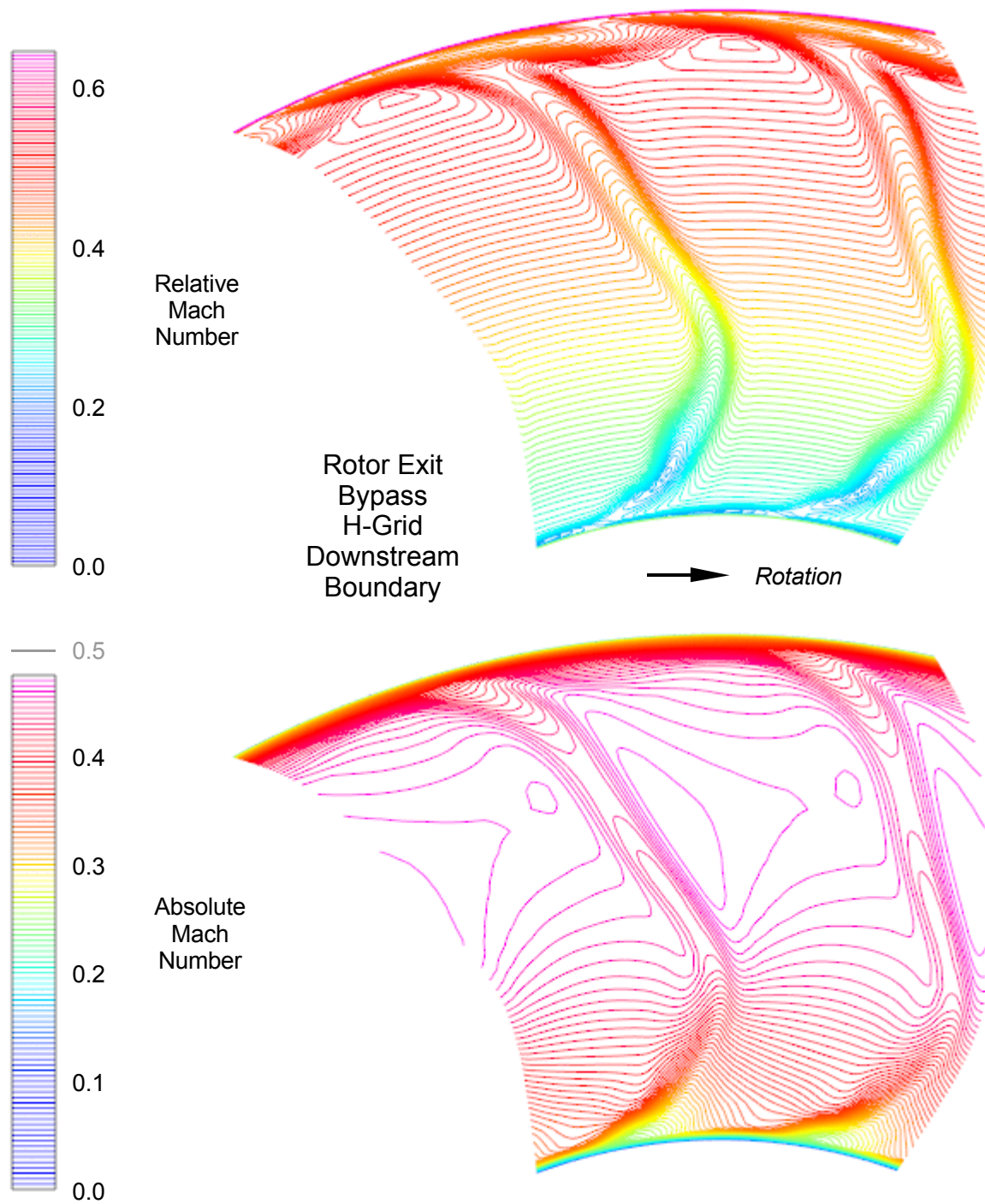
Figure 32a: *Computed Rotor Flow Field for the Cutback Operating Point; Downstream Mixing Plane; Relative and Absolute Mach Number Contours*
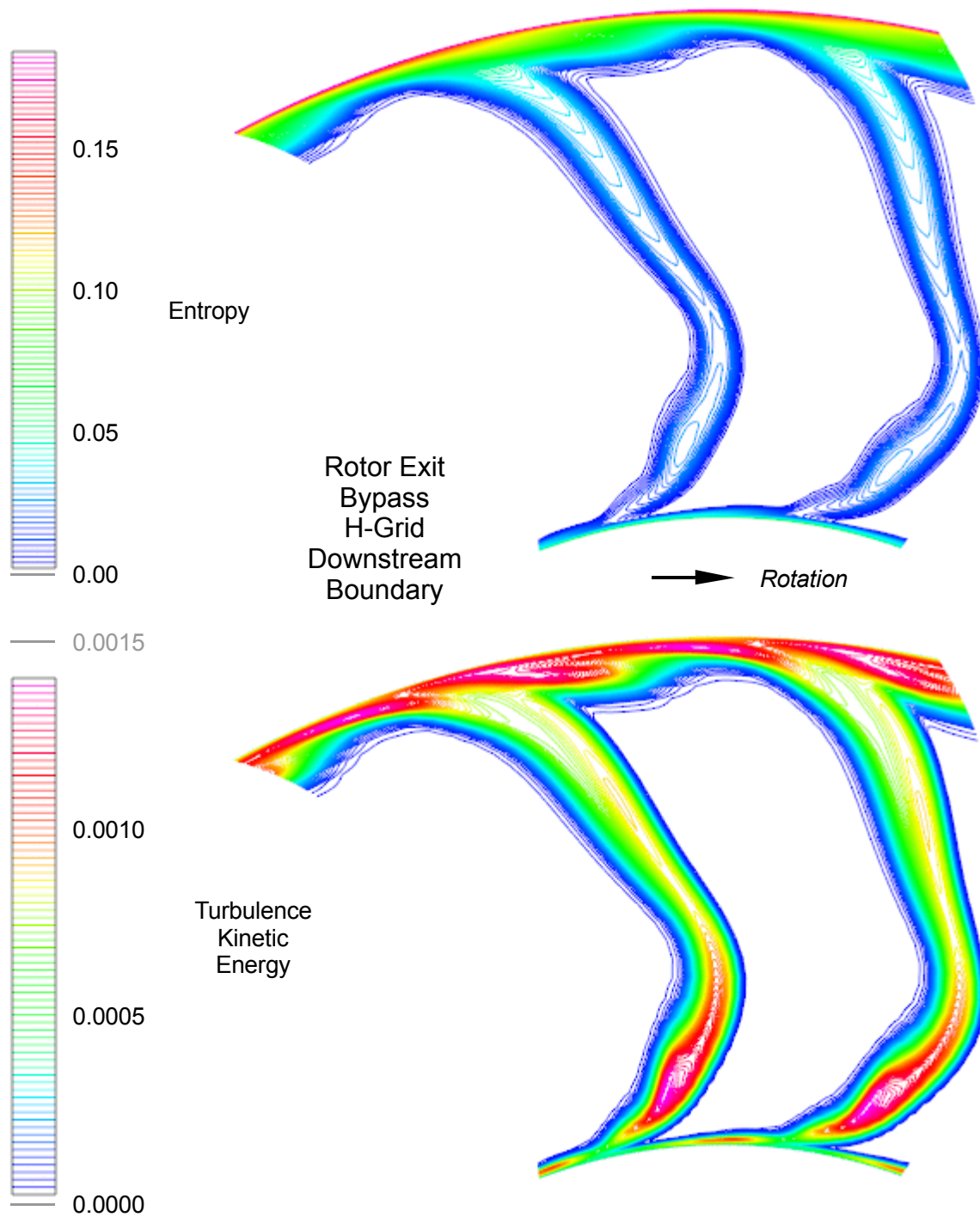
Figure 32b: Computed Rotor Flow Field for the Cutback Operating Point; Downstream
Mixing Plane; Entropy and Turbulence Kinetic Energy Contours

Approach Operating Point
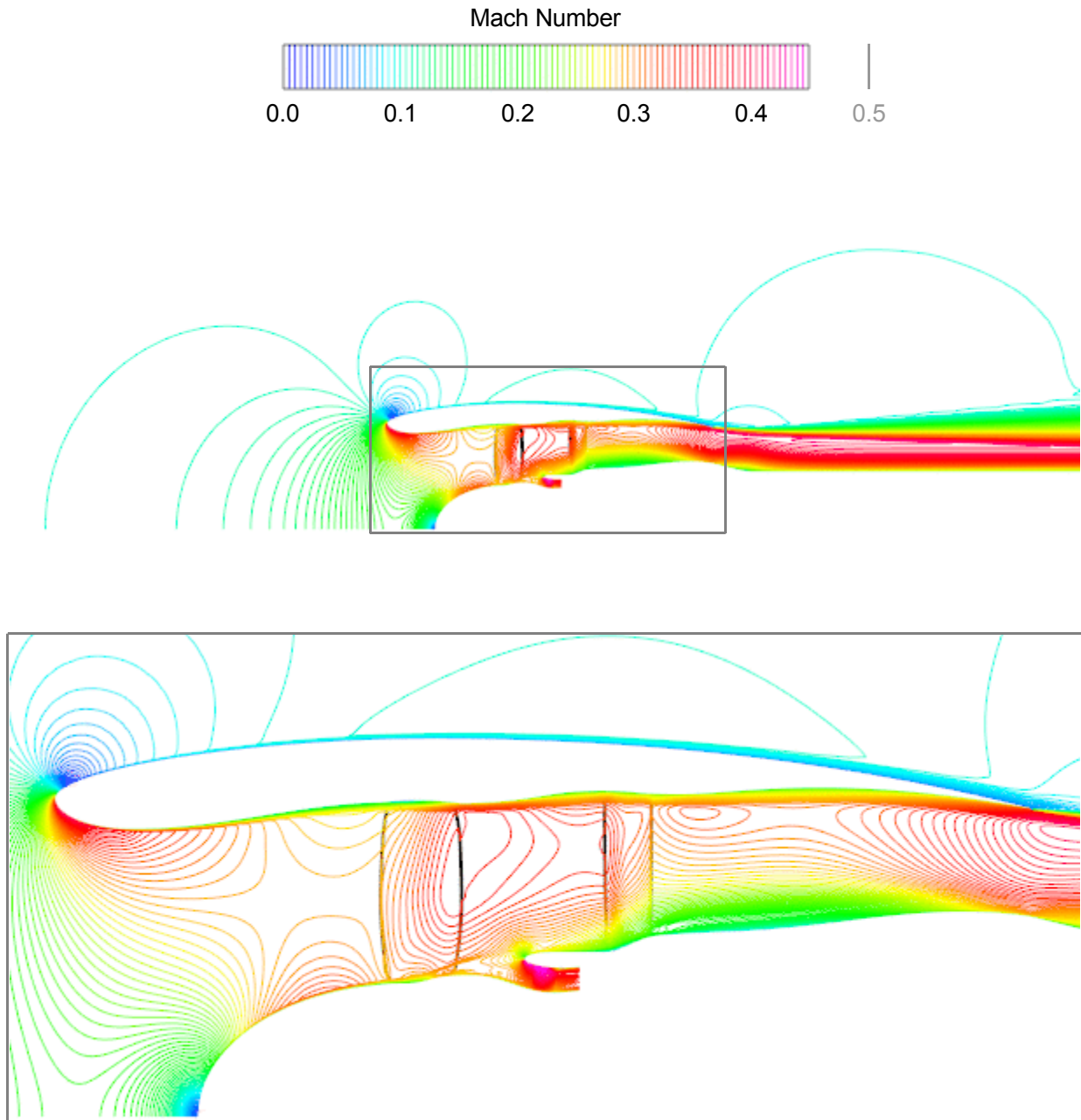
Figure 33: Computed Fan System Flow Field for the Approach Operating Point;
Pitchwise-Averaged Flow; Mach Number Contours
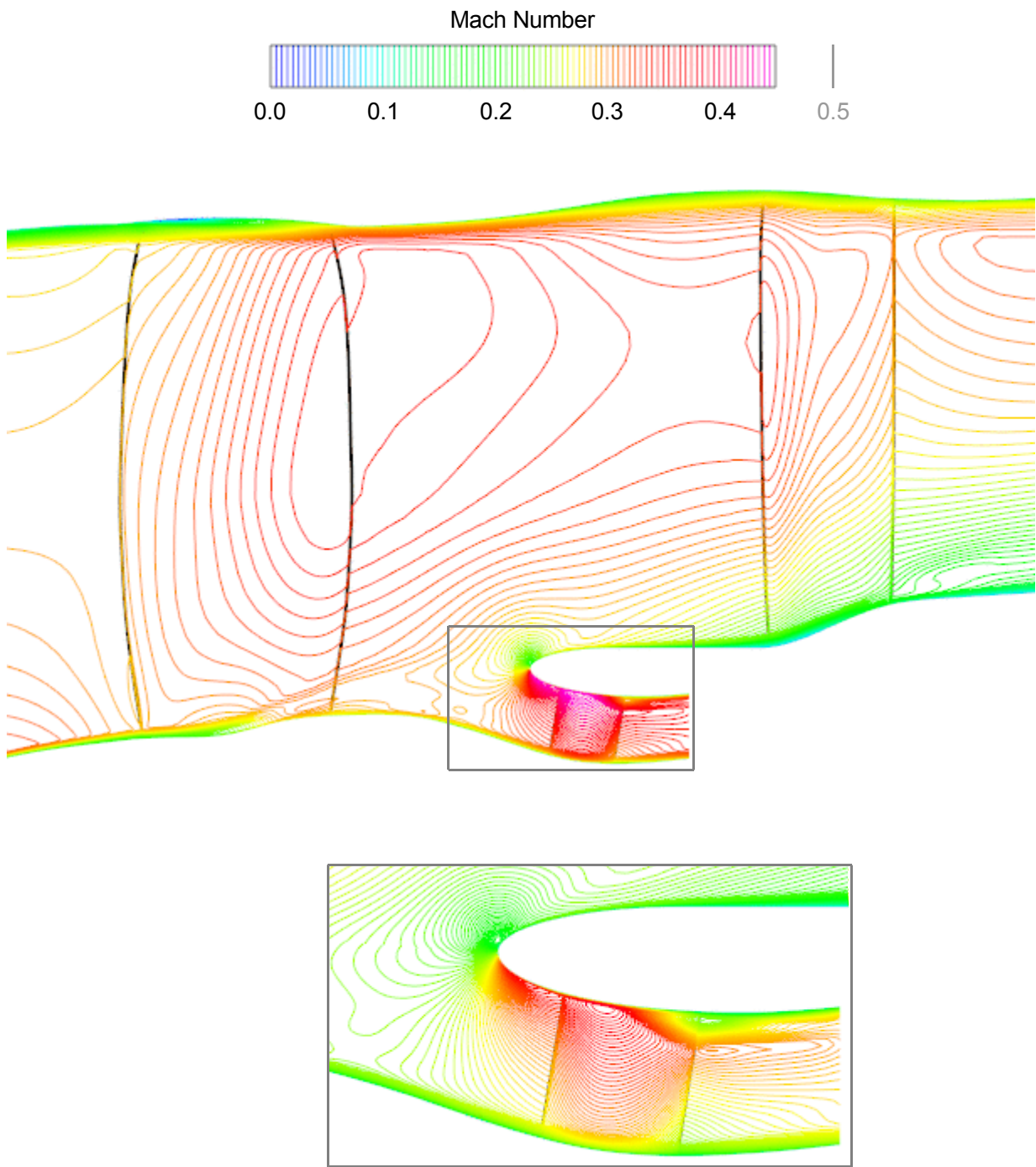
Figure 34: Computed Fan Blade Row Flow Fields for the Approach Operating Point;
Pitchwise-Averaged Flow; Mach Number Contours

Approach Operating Point
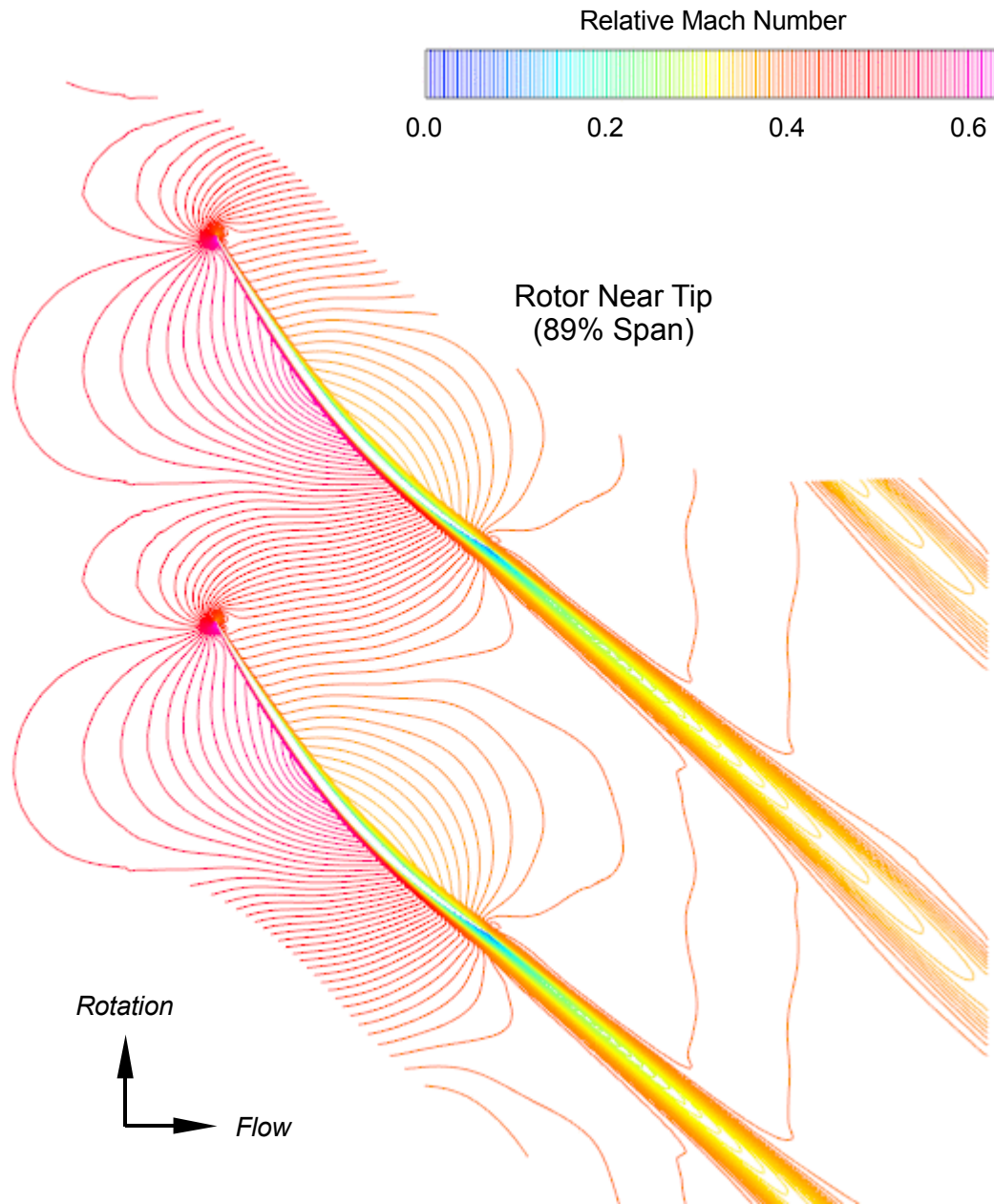
Figure 35a: Computed Rotor Flow Field for the Approach Operating Point;
Blade-to-Blade Relative Mach Number Contours

Rotor Near Mid
(51% Span)

Rotor Near Hub
(8% Span)
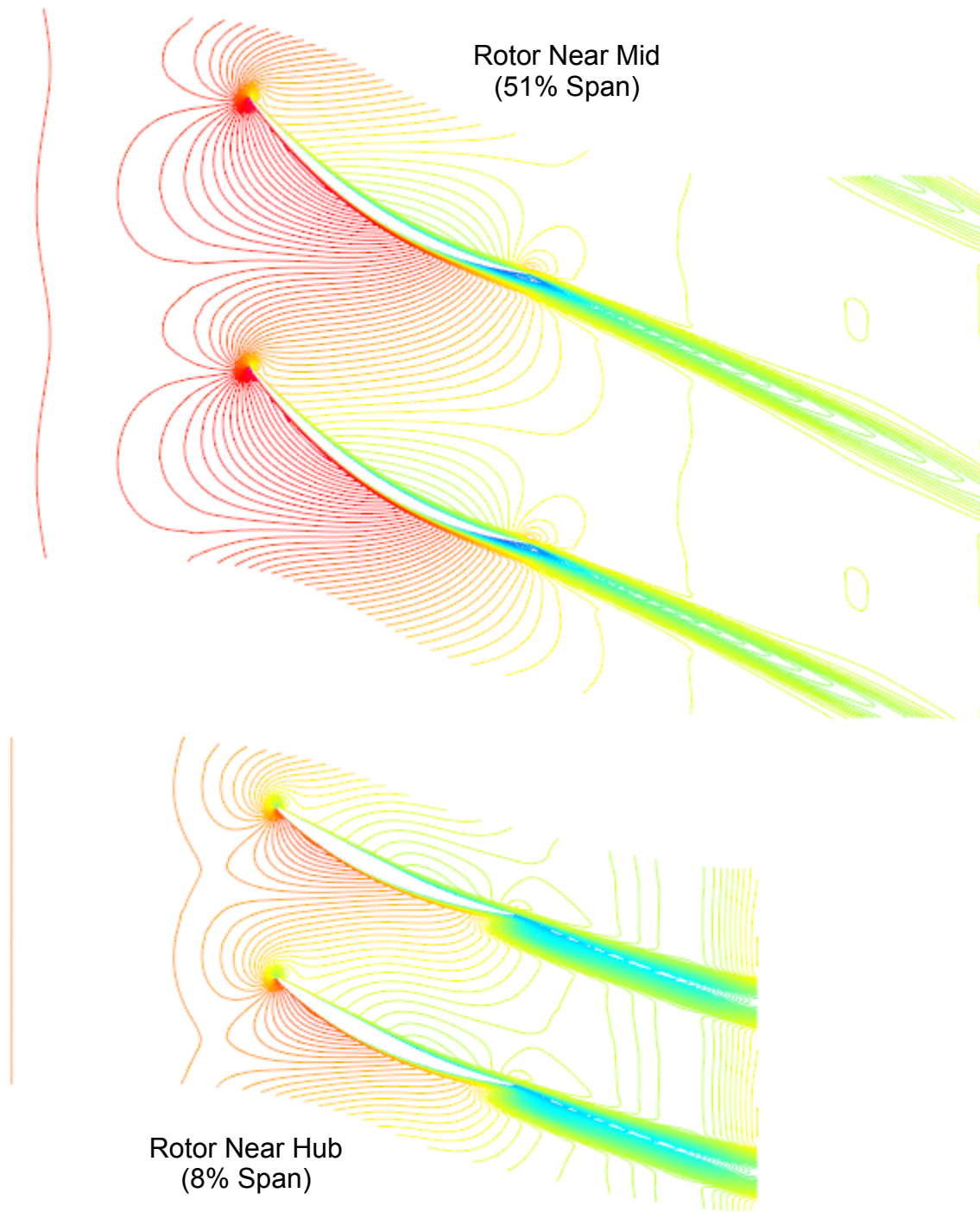
*Figure 35b: Computed Rotor Flow Field for the Approach Operating Point;
Blade-to-Blade Relative Mach Number Contours*
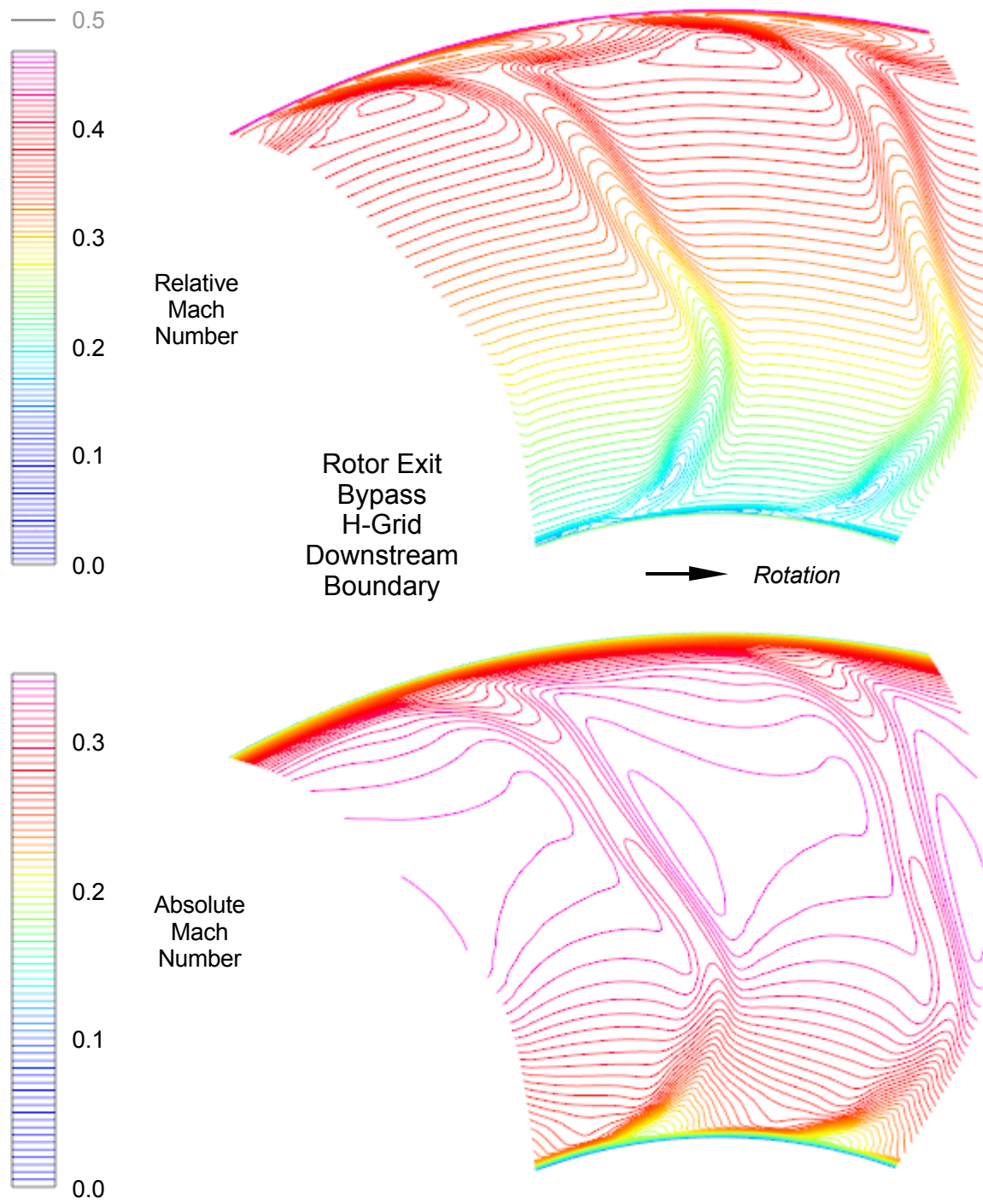
Figure 36a: Computed Rotor Flow Field for the Approach Operating Point; Downstream Mixing Plane; Relative and Absolute Mach Number Contours

The contour plots show scale bars with the following labels:

Entropy (top scale bar):
- 0.08
- 0.06
- 0.04
- 0.02
- 0.00

Turbulence Kinetic Energy (bottom scale bar):
- 0.0006
- 0.0004
- 0.0002
- 0.0000

Rotor Exit
Bypass
H-Grid
Downstream
Boundary

Rotation
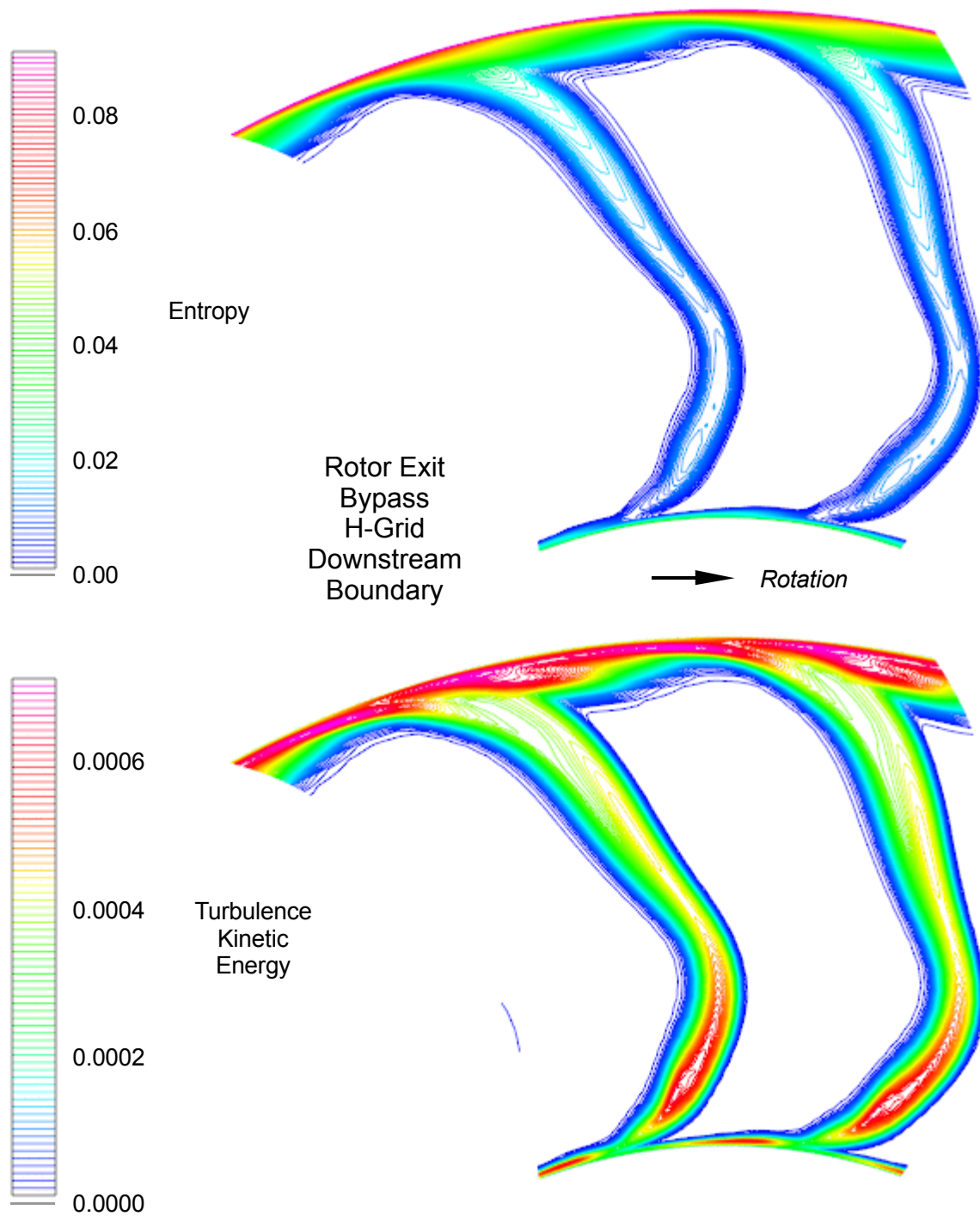
Figure 36b: Computed Rotor Flow Field for the Approach Operating Point; Downstream Mixing Plane; Entropy and Turbulence Kinetic Energy Contours

Approach Operating Point
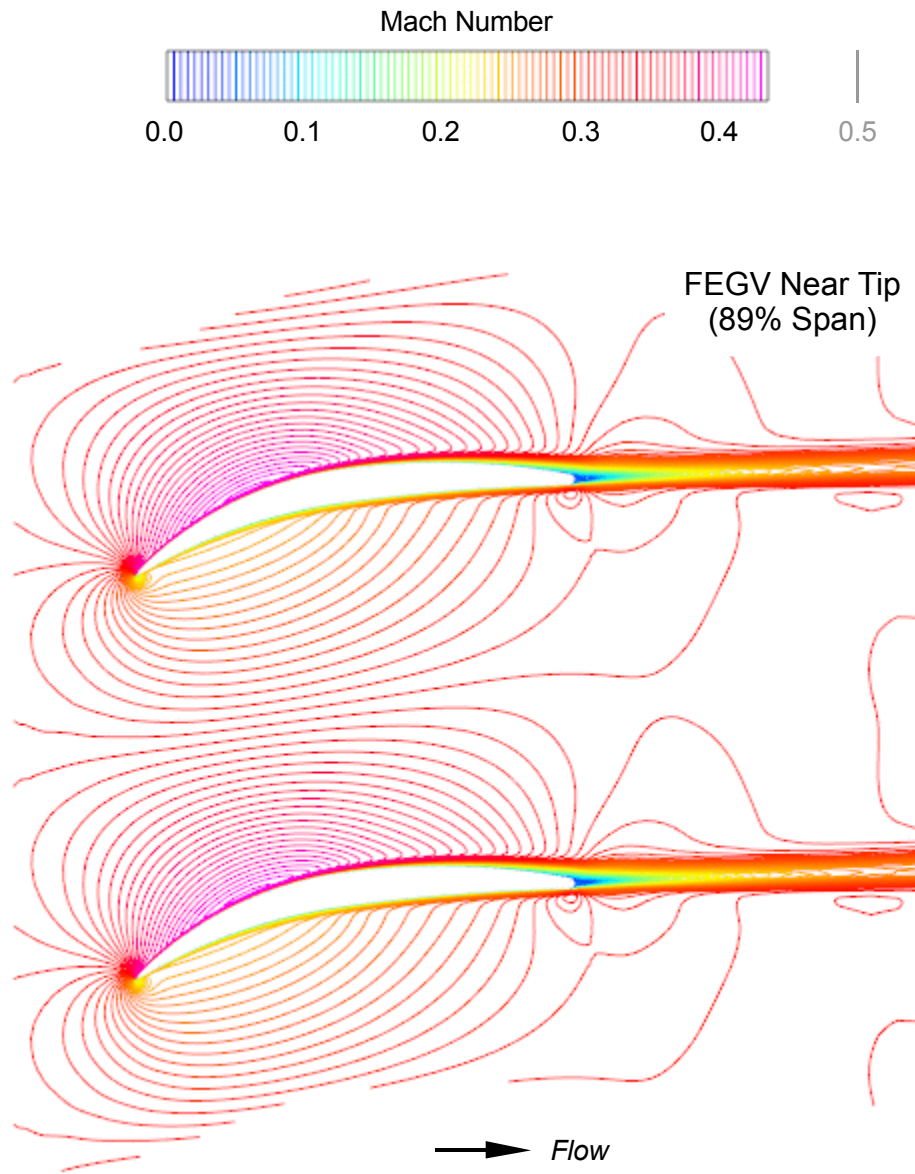
Figure 37a: *Computed FEGV Flow Field for the Approach Operating Point; Blade-to-Blade Mach Number Contours*

FEGV Near Mid
(48% Span)

Flow

FEGV Near Hub
(10% Span)
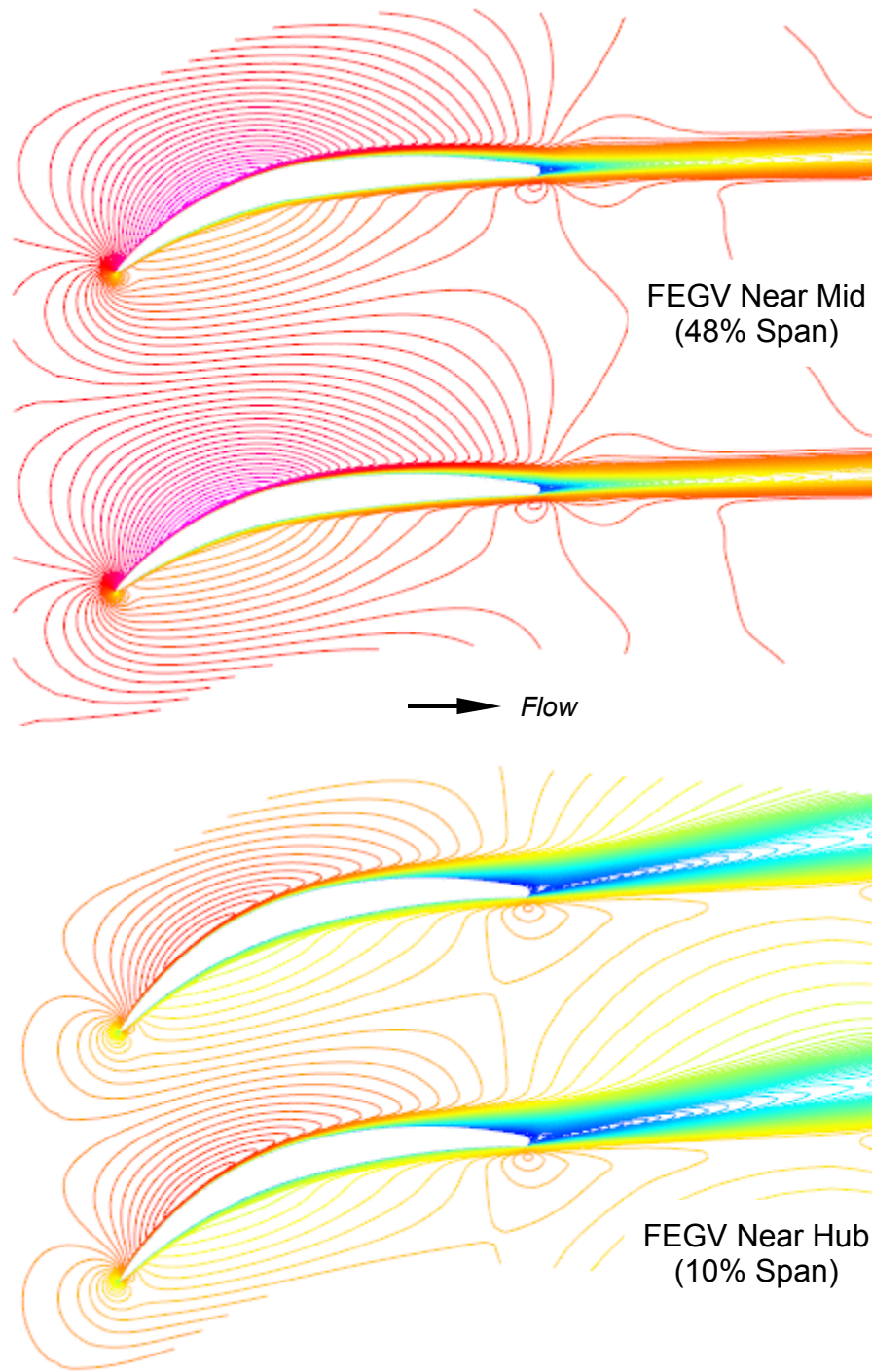
*Figure 37b: Computed FEGV Flow Field for the Approach Operating Point;
Blade-to-Blade Mach Number Contours*

FEGV C-Grid
Downstream
Boundary
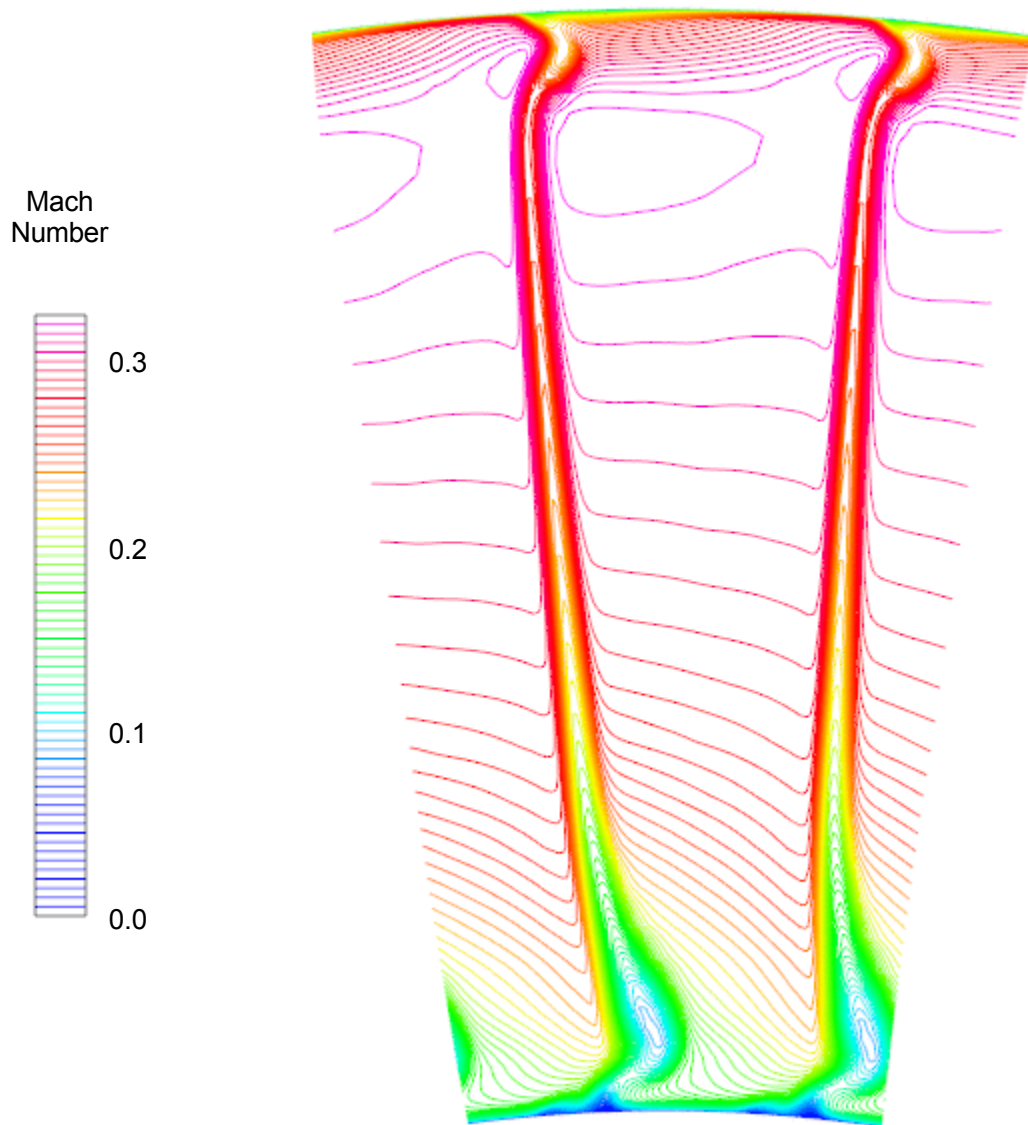
Mach
Number

Figure 38: Computed FEGV Flow Field for the Approach Operating Point;
Downstream Mixing Plane; Mach Number Contours

1. REPORT DATE (DD-MM-YYYY) 01-10-2014	2. REPORT TYPE Final Contractor Report	3. DATES COVERED (From - To)

4. TITLE AND SUBTITLE	5a. CONTRACT NUMBER
Computational Aerodynamic Simulations of an 840 ft/sec Tip Speed Advanced Ducted Propulsor Fan System Model for Acoustic Methods Assessment and Development	NNC06BA07B
	5b. GRANT NUMBER
	5c. PROGRAM ELEMENT NUMBER

6. AUTHOR(S)	5d. PROJECT NUMBER
Tweedt, Daniel, L.	
	5e. TASK NUMBER NNC07E190T
	5f. WORK UNIT NUMBER WBS 473452.02.03.07.06.01.06

7. PERFORMING ORGANIZATION NAME(S) AND ADDRESS(ES) AP Solutions, Inc.	8. PERFORMING ORGANIZATION REPORT NUMBER E-18897

9. SPONSORING/MONITORING AGENCY NAME(S) AND ADDRESS(ES) National Aeronautics and Space Administration Washington, DC 20546-0001	10. SPONSORING/MONITOR'S ACRONYM(S) NASA
	11. SPONSORING/MONITORING REPORT NUMBER NASA/CR-2014-218129

12. DISTRIBUTION/AVAILABILITY STATEMENT
Unclassified-Unlimited
Subject Category: 71
Available electronically at http://www.sti.nasa.gov
This publication is available from the NASA Center for AeroSpace Information, 443-757-5802

13. SUPPLEMENTARY NOTES

14. ABSTRACT
Computational Aerodynamic simulations of an 840 ft/sec tip speed, Advanced Ducted Propulsor fan system were performed at five different operating points on the fan operating line, in order to provide detailed internal flow field information for use with fan acoustic prediction methods presently being developed, assessed and validated. The fan system is a sub-scale, lownoise research fan/nacelle model that has undergone extensive experimental testing in the 9- by 15-foot Low Speed Wind Tunnel at the NASA Glenn Research Center, resulting in quality, detailed aerodynamic and acoustic measurement data. Details of the fan geometry, the computational fluid dynamics methods, the computational grids, and various computational parameters relevant to the numerical simulations are discussed. Flow field results for three of the five operating conditions simulated are presented in order to provide a representative look at the computed solutions. Each of the five fan aerodynamic simulations involved the entire fan system, excluding a long core duct section downstream of the core inlet guide vane. As a result, only fan rotational speed and system bypass ratio, set by specifying static pressure downstream of the core inlet guide vane row, were adjusted in order to set the fan operating point, leading to operating points that lie on a fan operating line and making mass flow rate a fully dependent parameter. The resulting mass flow rates are in good agreement with measurement values. The computed blade row flow fields for all five fan operating points are, in general, aerodynamically healthy. Rotor blade and fan exit guide vane flow characteristics are good, including incidence and deviation angles, chordwise static pressure distributions, blade surface boundary layers, secondary flow structures, and blade wakes. Examination of the computed flow fields reveals no excessive boundary layer separations or related secondary-flow problems. A few spanwise comparisons between computational and measurement data in the bypass duct show that they are in good agreement, thus providing a partial validation of the computational results.

15. SUBJECT TERMS
Low noise; Models; Scale models; Turbofans; Acoustic measurement; Aerodynamic

16. SECURITY CLASSIFICATION OF:			17. LIMITATION OF ABSTRACT	18. NUMBER OF PAGES	19a. NAME OF RESPONSIBLE PERSON STI Help Desk (email:help@sti.nasa.gov)
a. REPORT U	b. ABSTRACT U	c. THIS PAGE U	UU	60	19b. TELEPHONE NUMBER (include area code) 443-757-5802